The influence of RNA-RNA Interaction on the Formation Kinetics of Biomolecular Condensates

Abstract

Compartmentalization is one of the most essential aspects of cellular organization and makes life as we know it possible. Traditionally, we think of cell walls or cell membranes as tools for organizing cells, but membrane-less organelles form a less well-known, but equally important aspect of organization. In this project, we use the rapidly emerging field of microfluidics to study the liquid-liquid phase separation of the yeast Dhh1 protein in a dynamic environment, with the ultimate goal of illuminating the influence of RNA-RNA interactions on the kinetics of condensate formation. We first determine ideal conditions for live on-chip imaging using classical phase separation assays. Next, we design and produce a microfluidic chip from the ground up, taking into account previous experience and projects by groups also working on microfluidics. We show important attributes of the new chip models by droplet-generating experiments using fluorescent chemicals. Subsequently, we explore the temporal kinetics of phase separation by imaging protein condensate containing droplets generated by our chip and captured in a capillary. Finally, we show our attempts to image phase separation live while simultaneously trying to work out issues with the chip. During the project we built a strong foundation for future inroads into microfluidics and liquid-liquid phase separation experiments.

Table of contents

Contents

List of tables

List of figures

Materials and Methods

Figure 16 – Illustrations of designs that were not used for the current experiment but could be used for future ones.

List of abbreviations

AMP – Ampicillin

CAM – Chloramphenicol

CNT – Classical Nucleation Theory

DDX – RNA-dependent DEAD-box ATPases

DoE – Design of Experiment

HFE-7500 – 3M™ Novec™ 7500 Engineered Fluid

IMAC – Immobilized Metal Affinity Chromatography

IPTG – Isopropyl β-D-1-thiogalactopyranoside

LB – Lysogeny Broth

LCD – Low-Complexity Domain

LLPS – Liquid-Liquid Phase Separation

LOC – lab-on-a-chip

MLOs – Membraneless Organelles

OD – Optical Density

P-Body – Processing Body

PDMS – Polydimethylsiloxane

SDS-PAGE – sodium dodecyl sulfate-polyacrylamide gel electrophoresis

SEC – Size Exclusion Chromatography

STD – Standard Deviation

TB – Terrific Broth

Introduction

Cellular processes in Eukaryotes became evolutionarily highly compartmentalized.[1] Without this form of spatial organization, life in its current form would not be possible due to the high level of specificity required for cellular processes, such as ATP production in the mitochondria.[2] Intracellular compartmentalization can take different forms, such as gradients[3], physical separation such as organelles and their lateral diffusion barriers[4] or protein interactions[5]. Of particular interest to us were so-called membraneless organelles (MLOs) that result from liquid-liquid phase separation (LLPS). A wide range of different MLOs have been identified, such as the nucleolus[6], Cajal bodies[7], nuclear speckles[8], paraspeckles[9], promyelocytic leukemia protein (PML) nuclear bodies[10], nuclear stress bodies[11], processing bodies (P-body)[12] and stress granules[13]. In this thesis, we focused on Dhh1, an RNA dependent DEAD-Box ATPase in yeast.[14], which are widespread and varied regulators of phase separation.[15] Their structure is highly preserved, and the name DEAD-box itself derives from an amino acid motif found in the catalytic core, where ATP hydrolysis occurs. Other than the name giving D-E-A-D motif, 8 more highly conserved can be found. From the N-terminus to the C-terminus, those motifs are Q-motif, motif 1, motif 1a, motif 1b, motif II, motif III, motif IV, motif V and motif VI. It has been demonstrated that DDXs promote phase separation in their ATP-bound form, but induce compartment turnover and RNA release upon ATP hydrolysis.[16] This mechanism is almost the same from bacteria to humans.

The protein Dhh1, first described by *Strahl-Bolsinger et al.* in 1993[17] has been implicated as a degradation factor of mRNA by decapping in yeast.[18] The human analogue to Dhh1 is DDX6. Degradation of mRNA is an essential part of cellular function, as control of gene expression keeps protein production inside the cell under control. Without regulation, mRNA could be translated endlessly. While translation can be arrested without degradation of the mRNA[19], degradation remains the most important method of doing so. Dhh1 consists of a globular core with two RecA-like domains that can bind RNA and ATP. RNA–protein interactions are governed by electrostatic interactions between the phosphate backbones of the RNA and a positively charged cleft on the RecA domains.[20] They are connected by a linker and in some cases flanked by two low-complexity domains (LCDs).[21] (**Fig. 1a**) LCDs are regions usually consisting of a primary amino acid and a less common secondary amino acid. Research into these LCDs is still ongoing to uncover the effects of their unique biophysical properties on proteins.[22]

Materials and Methods
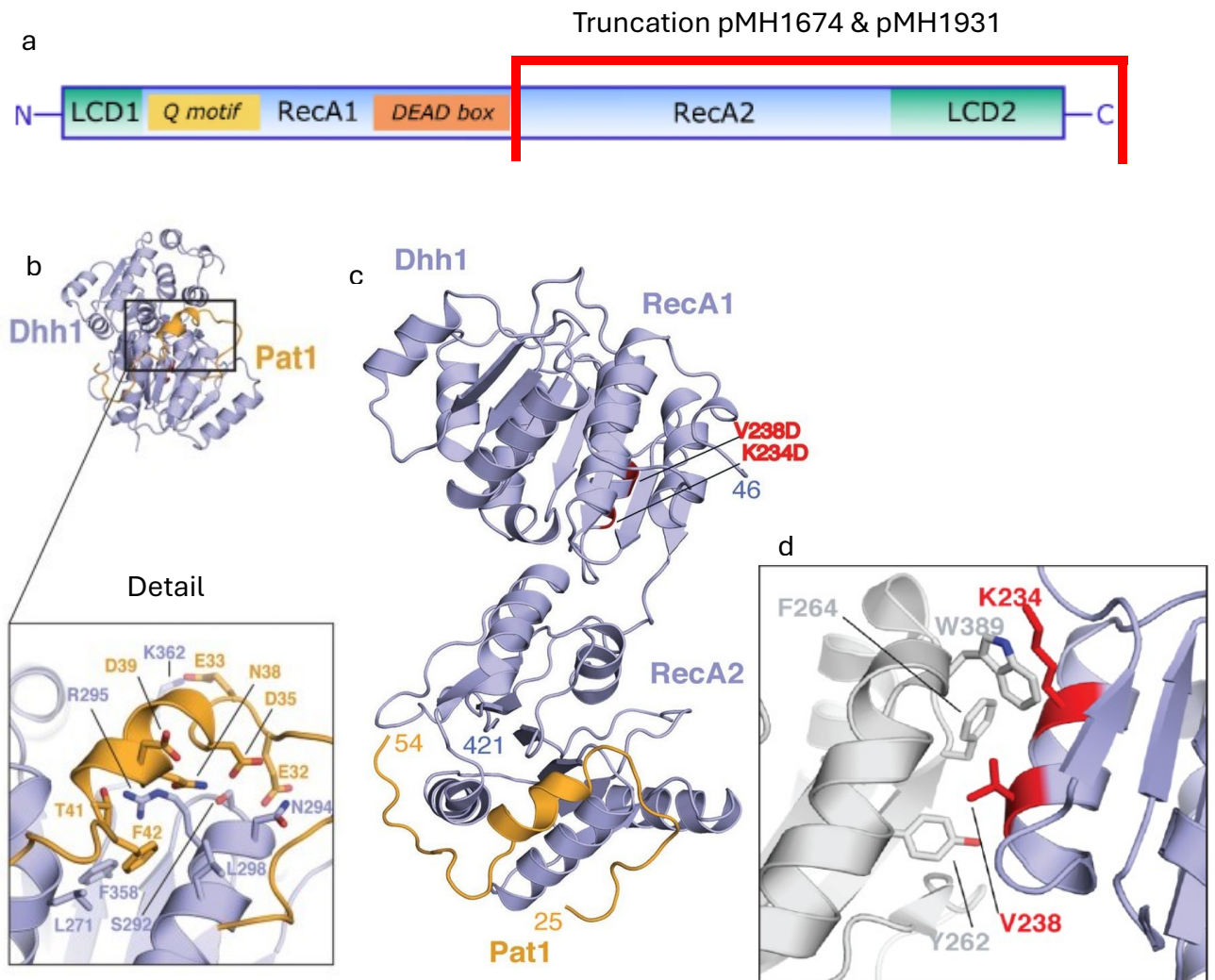
Figure 1: *a. The full-length Dhh1 with its two RecA domains flanked by two LCDs. Image adapted from Linsenmeier et al., 2022. b. The structure of a Dhh1-Pat1 complex (above) and details on their interaction site (Detail). The mutations for pMH1930 and pMH1931 were done on S292, N294 and R295. Image adapted from Sharif et al., 2013. c. The structure of the Dhh1-Pat1 complex with the point mutations used in pMH1806 (V238D and K234D) highlighted in red. Image adapted from Sharif et al., 2013. d. More detail on the site of V238 and K234. The gray structure shows the intermolecular interaction of another RecA2 domain with the RecA1 domain containing the highlighted amino acid side chains. Image adapted from Sharif et al., 2013.*

The mentioned RNA-protein interactions were of particular interest to us, as they were implicated in being a major influence on LLPS kinetics.[23] For this reason, an initial LLPS assay sought to confirm the strong influence of RNA on LLPS. 3 different Dhh1 mutations were prepared. The first protein was a truncated version of the Dhh1-WT, containing amino acids 250-505, with only the RecA2 domain and the C-tail remaining, designated pMH1674. The other two proteins were based on the paper by *Sharif et al.*, 2013[24], containing point mutations at 3A S292D, 3A N294D and 3B R295D, which reduce interaction of Dhh1 with Pat1 (**Fig. 1b**). Pat1 is important for P-body assembly by enhancing phase separation of Dhh1.[25] The first mutated protein was designated pMH1930, while the other, which was additionally truncated like pMH1674, was

designated pMH1931. After confirming the influence of RNA, subsequent experiments used another protein described by *Sharif et al.*, 2013, designated pMH1806, which contained the point mutations K234D and V238D. (**Fig. 1c**) This mutation prevented intermolecular RecA1-RecA2 interaction and thus reduced non-phase separation clumping of the protein (**Fig. 1d**). After determining ideal RNA conditions using a LLPS assay, it was planned to use artificially designed RNA fragments with predicted interaction energies to investigate whether these interaction energies influence LLPS formation kinetics.

The tool chosen for this advanced analysis was microfluidics. Defined as manipulation of fluids at the submillimeter scale, microfluidics has come a long way as an investigative resource in biological research. Among the first practical applications of microfluidics was the creation of a miniaturized gas chromatograph on a silicon wafer by *Terry et al*. in 1979[26]. The principle was refined further by *Menz et al*. in 1993 to create one of the first lab-on-a-chip (LOC) systems, downscaling a chemical analysis system.[27] The Lab-on-a-chip concept, in which several laboratory functions can be combined into a small-scale system, was however still in its infancy, as lithographic methods were complicated and time-consuming. Photolithographic methods were most suited for semiconducting materials, further reducing utility in biological applications. This problem was solved by soft-lithography, using elastomeric molds to transfer patterns instead of photomasks. Another important improvement was the utilization of Polydimethylsiloxane (PDMS), based on siloxanes first characterized by Kipping in 1927. PDMS as a material for microfluidics was popularized by *Whitesides et al*. in 1998.[28] Desirable aspects of PDMS include its opacity and easy-of-use, while also allowing permeability of gases, important for biological research. PDMS remains a popular and widespread material for the creation of microfluidic chips and was used in this project. Outside utilizing precise mixing of interacting fluid streams, which was used in this thesis, microfluidics has found application in next-generation genomic sequence analysis, diagnostic tests and even single-cell analysis.[29] Distinctly different from macroscopic processes, effects such as gravity, surface tension and capillary forces have markedly different impacts on fluids on the microscopic scale. An often exploited factor in continuous flow microfluidic experiments is the characteristically low Reynolds number, which indicates an essentially laminar flow of phases.[30] This makes unique experimental environments possible, such as precise gradient control for cell migration experiments.[31] While the mentioned continuous systems have trouble scaling up, droplet based systems have no such issues. However, additional considerations must be made when creating a droplet based microfluidic system. The T-junction, where the droplets are created from the phases, can

have various different forms with pronounced effects on the droplets. Factors such as viscosity, surfactant usage and hydrophobia and hydrophilia of the channel surface can strongly influence droplet characteristics as well. These phenomena can also be effectively deployed for a wide range of other tasks, such as passively pumping fluids in microchannels, patterning surfaces with custom substrates, analyte filtering or forming monodisperse droplets.[32] In this thesis, it was planned to establish a reliable and easy-to-use microfluidics system in order to visualize LLPS directly on-chip. The design of the chip was an important factor to ensure proper mixing and thus homogeneity of the protein-containing droplets, but also to prevent protein clumping and overtly high droplet velocity. Thus, multiple wafer designs and chip manufacturing processes were iterated to ensure the best possible result.

Enclosing protein in homogenous droplets was picked as an ideal method to observe condensate formation. It was theorized that the condensate formation would follow the Classical Nucleation Theory (CNT). Verifying the theory for the Dhh1 condensate formation was one of the goals of the project. CNT is the most common model to study the kinetics of nucleation and models the timeframe for the formation of a new phase. The theory assumes that unstable nuclei form a metastable condensate at an energy
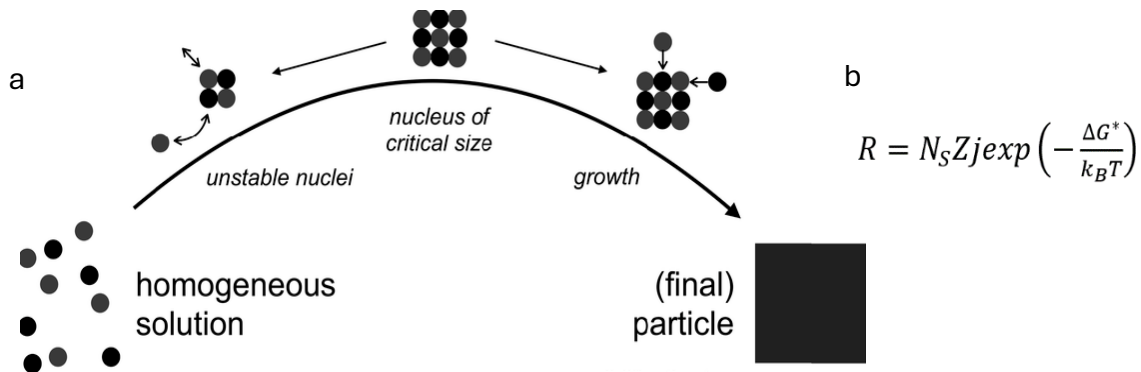
Figure 2: *a*. An illustration showing the steps of condensate formation according to CNT. *b*. The basic formula of CNT.

threshold. (**Fig. 2a**) If this barrier is crossed and the condensate does not dissolve again, growth occurs and a final particle is formed. The basic version (**Fig. 2b**) predicts a rate of nucleation R in the units $m^{-3}s^{-1}$, meaning the number of nucleation events in a 1 cubic meter per second. N_S represents the number of nucleation sites, Z is the Zeldovich factor, which gives the probability that a nucleus at the energy threshold forms a new phase instead of dissolving, j is the rate of molecules attaching to the nucleus and $\frac{\Delta G^*}{k_B T}$ is the free energy cost of the nucleus at the energy threshold divided by temperature T times the Boltzmann factor k_B. From this it is apparent that the discrete volume of a microfluidic droplet represents an ideal solution to test CNT.

Materials and Methods

Master Wafer Production

The microfluidic chips were designed in SolidWorks® (Dassault Systèmes SE®) and the corresponding thin-film photomasks produced by Selba S.A®. The wafers were created in the D-BSSE Clean Room Facility. Si-Mat Silicon Materials® Si-Wafers (P/Bor<100>±0.5°, diameter 100±0.2 mm, thickness 525±25 μm) were heated to 200°C on a hotplate for 5 minutes. After a short cooldown, the wafers were put on a spin-coater and 7 ml of Kayaku®SU-8 3050 (Product Item #: Y311075 05001GL) photoresist was deposited in the middle. After accelerating to 500 rpm after 5 seconds, the wafer was spun at 4000 rpm according to manufacturer protocol (**Fig. 3**). Spinning at 4000 rpm for 30 seconds resulted in an average channel thickness of 38.6±0.1 μm, at 5000 rpm in 37.9±0.4 μm. As the difference between the two wafer spin speeds was only 0.7 μm in

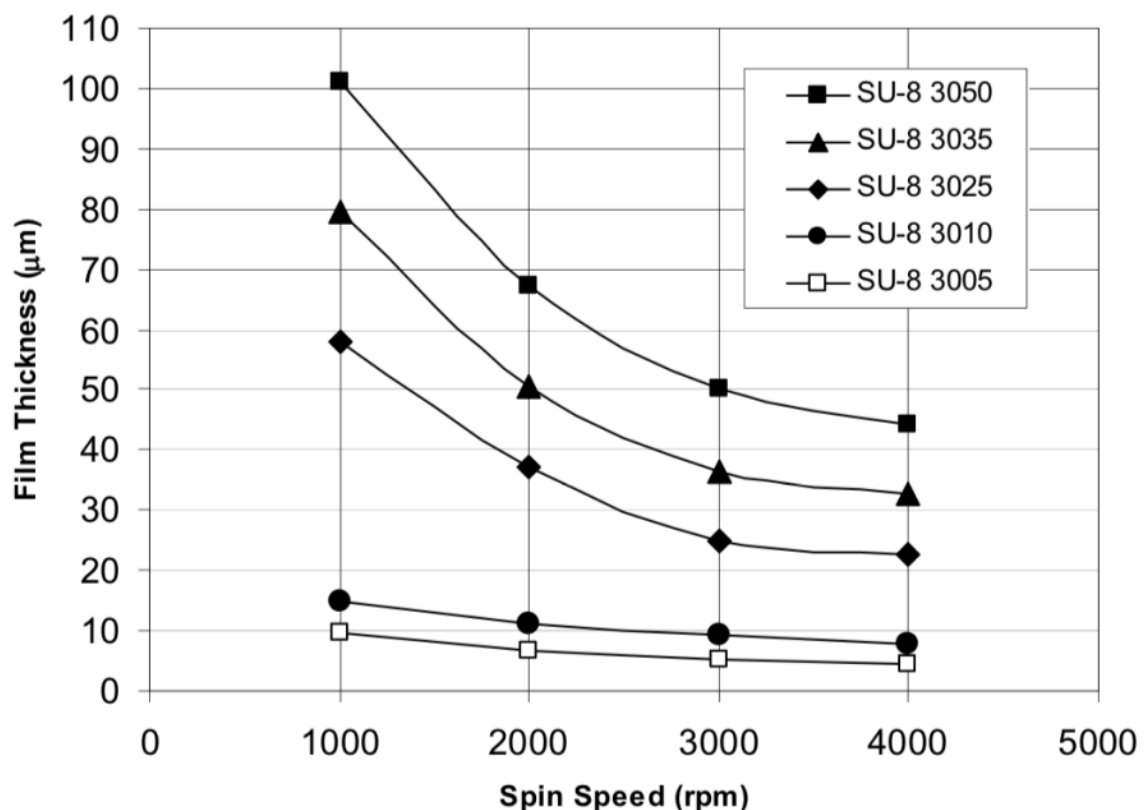*Figure 3: The channel thickness of the SU8-3000 photoresist series depending on spin coater rpm. Adapted from https://kayakuam.com/wp-content/uploads/2020/07/KAM-SU-8-3000-Datasheet-7.10-final.pdf*

wafer thickness, the final design used a spin speed of 3500 rpm. This resulted in an average thickness of 39.3±3.1 μm. The coated wafers were left on covered leveling plates

for 30 minutes, after which they were soft-baked for 1 minute at 65°C and 15 minutes at 95°C. The UV exposure was done in a Süss MicroTec® MA/BA Gen 4 Mask aligner at 300 mJ/cm^2. Later, forgoing the UV masks, a Heidelberg® MLA 150® Maskless lithography system was used. A post-exposure bake was done for 1 minute at 65°C and 5 minutes at 95°C. Using the automatic developer, the non-crosslinked SU-8 photoresist was washed off and the wafer was hard-baked for 5 minutes at 150°C. After some issues with plastic adhering to the wafer surface, the wafers were treated with Sigma Aldrich® Trichloro(chloromethyl)silane (Product no. 8.42025). 1 mL was taken up by a syringe and deposited into an aluminum foil receptacle. This receptacle was placed in an airtight container together with the wafers and left under a fume hood for an hour. The coated finished wafers were inserted into a glass petri dish.

PDMS Chip Production
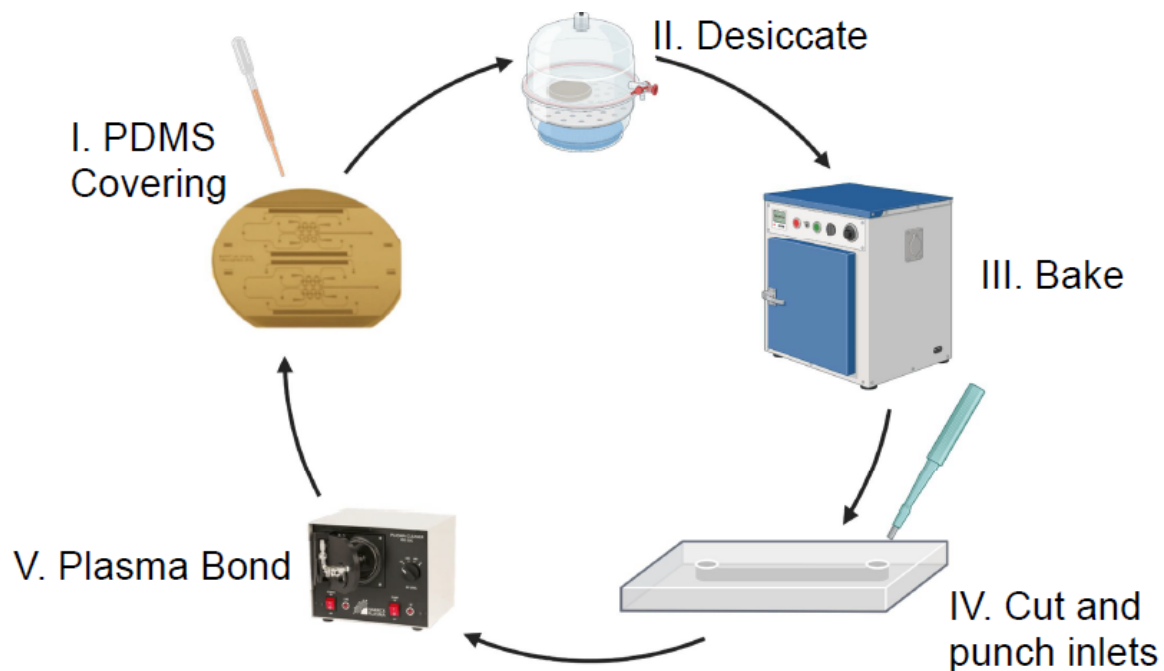
Figure 4: The cycle of PDMS microfluidic chip production: First the chips are covered in PDMS (I), then desiccated (II) and baked (III). The hardened PDMS is then cut off from the wafer and individual chips are made (IV). Finally, the chips are bonded to glass slides using a plasma oven (V).

For the production of the chips (**Fig. 4**), we used Dow Corning® SLYGARD™ 184 Silicone Elastomer Kit (GMID: 01673921), where Silicone Elastomer Base was mixed with the curing agent at a ratio of 10:1. The mixture was stirred for 2 minutes and poured into the petri dish containing the wafer. After waiting for 30 minutes in order to dissipate air bubbles that occurred during the stirring, the mixture was further treated in a desiccator. The pressure was lowered to around 50 mbar, after which the vacuum pump was stopped until the bubbles popped. This process was repeated 2 more times. The mixture was then cured at 85 °C for 1 hour in an oven. With the PDMS layer hardened, the layer was cut out

and the structured side was protected by scotch tape. After cutting the layer into appropriate chips, 0.75 mm sized holes were made in the designated inlets and outlets using a biopsy puncher. Next, the chips and cover slips (Epredia® cut microscope slides, Ref AA00000102E01MNZ20) were cleaned using isopropanol and Millie-Q®, dried and put into a plasma oven (Harrick Plasma® Plasma Cleaner PDC-32G) for 1 minute at a pressure of 2 mbar. The chips and slides were then bonded and heated at 95 °C for 2 hours, but this duration was cut down to 1 hour during later experimentation. There was no notable difference in consistency or wafer adherence for both durations.

Classic LLPS Assays

The LLPS assay for the pMH1674, pMH1930 and pMH1931 were conducted using a classical dilution series. The master mix (**Appendix table 1**) contained buffer solution (no NaCl), 0.5 mg/mL BSA, 1 mM ATP, 0.05 mg/mL PolyU, MilieQ and 25 mM Phosphate buffer at pH = 6.4. 2 µL of the diluted protein was deposited on the side of the well and 18 µL of the mentioned buffer were pipetted up and down, mixing with the protein droplet. After ensuring no bubbles occurred, the wells were imaged using the Ti2-E™ Microscope. Each well was imaged 4 times from each corner.

For the Design of Experiment (DoE), 19 different conditions were tested. This included 16 actual combinations and a triplicate for testing purposes. The combined final volume consisted of a salt containing buffer (0, 50 or 100 mM NaCl), 10 mg/mL BSA, 10 mM ATP, 1 mg/mL PolyU, elution buffer, MilieQ water and 100 mM Phosphate at pH level 6.4, 6.8 and 7.2. Besides the testing triplicate, 16 different combinations were prepared according to the DoE program (**Appendix Table 2**). 2 µL of Protein concentrated at 5 µM were carefully deposited on the side of the well plate wall. Subsequently, 18 µL of the assay mixture were taken up using a pipette and mixed with the protein on the wall by pipetting up and down. The combined 20 µL droplet then slid down to the bottom of the well. The contents of the wells were visualized at 20 °C using the Ti2-E™ Microscope. Each well was imaged 4 times from each corner.

Non-LLPS Droplet Generation and LLPS Capillary Experiments

Before starting the experiment, the chips were flushed with a mixture of 1% v/v of Trichloro(1H,1H,2H,2H perfluorooctyl)silane (Sigma-Aldrich®, 448931-10G) in 3M™ Novec™ 7500 Engineered Fluid (3M™ Novec™, 7100025016) (HFE-7500) and heated at 95 °C for 1 hour. To ascertain some basic droplet characteristics like droplet diameter,

homogeneity and velocity, fluorescent solutions simulating the LLPS trigger and protein solutions were used. To simulate the LLPS trigger solution, 126.5 µM Fluorescein in 1 mL of MilieQ water was used. To simulate the protein solution, 126.5 µM Rhodamine was dissolved in 1 mL of 1/3 Glycerol and 2/3 MilieQ water. For actual LLPS experiments, three solutions were prepared. The used oil solution was 5% w/w Pico-Surf™ in HFE-7500 (Sphere Fluidics™, Co22). This solution was further diluted using the HFE-7500 fluid to 0.5% v/v. For the live on-chip imaging experiments, a 1% v/v oil solution was used. Based on LLPS assays (See **Results and Discussion**), the trigger solution contained 4 mM MgCl2, 175 µL MilieQ water, 316.25 µM Fluorescein, 0.1 mg/mL PolyU, 1 mg/mL BSA and 500 µL mM Phosphate Buffer pH = 6.4. The concentration of the protein was determined using a ThermoScientific™ NanoDrop One/OneC Spectrophotometer. Dhh1-K234D-V238D was diluted to a concentration of 10 µM in 400 mM NaCl. 1% of Dhh1-K234D-V238D was labelled using ATTO-TEC® GmbH ATTO 565 fluorescent label dye according to the manufacturer's instructions.

For droplet generation, 3 Cetoni® Nemesys-S® syringe pumps were used. Before starting the experiment, the syringes were manually loaded using a pipette and flushed, so that no air bubbles remained in the syringes or the tubing. To analyze droplet diameter, homogeneity and velocity, the previously described rhodamine, fluorescein and Oil solutions were used. The tubing was inserted directly into the inlet holes and the chip flushed with the oil solution at a flow rate of 3 µl/min. Afterwards, the oil flow was stopped and both the flow of rhodamine and fluorescein solution was started at 1 µl/min. Once proper flow was verified using live microscope imaging, the oil flow was restarted at the same rate as before and the beginning of the 1 mm outlet channel was imaged, with both GFP and mCherry channels. For diameter and homogeneity, 10 images every 10 seconds were taken to ensure each image contained a complete turnover of generated droplets. To calculate the velocity, 50 images every 100 ms were taken.

To further explore the mechanics of LLPS, the experiment was repeated, this time using the described oil, trigger and protein solutions. The salt concentration was varied, with values ranging from 200 mM to 250 mM NaCl. Establishing the flow with the same parameters used by the non-LLPS fluorescent dyes, 0.1 mm Fabrinet® VitroCon® Rectangle Boro Tubing 0.1 x 2 mm ID capillaries (Catalogue Nr. 5012-050) were used to take up droplets for visualization using the Nikon™ Eclipse Ti2-E™. After establishing a flow and droplet generation, 10 or 15 different positions on the capillary were picked (to prevent bleaching out) and imaged in 1-minute intervals.

A Z-stack was created around the focus plane, consisting of 17 images (±8 around the focus plane) in steps of 2 µm. The time immediately after the capillary was applied to the

Materials and Methods
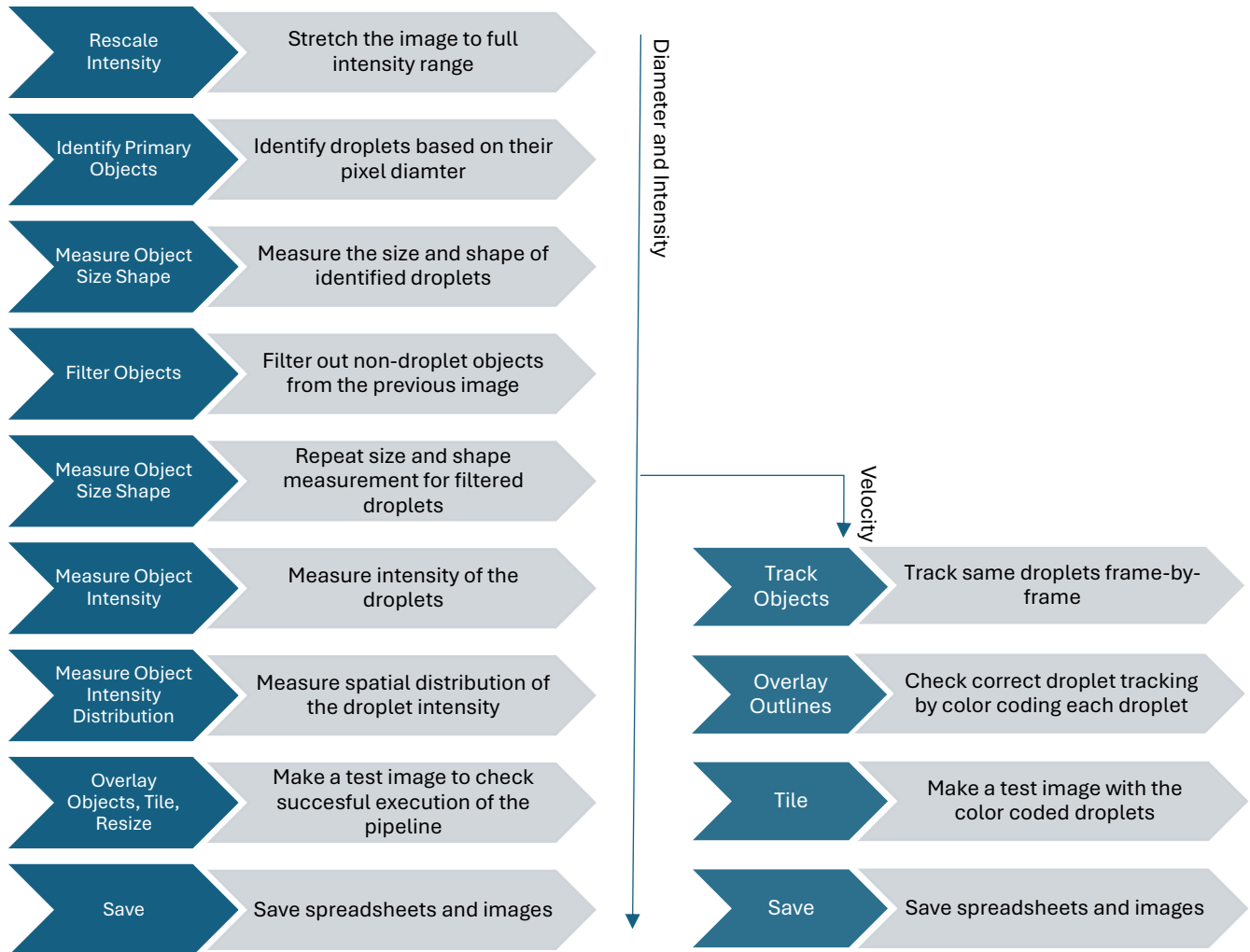
Image Analysis

Figure 5: Flowchart showing the chronological order of the CellProfiler Pipeline modules used for measurements of diameter, intensity and velocity.

For the exact CellProfiler settings used in the image analysis, see **Appendix Figure 3**. For analysis, the diameter and homogeneity images were background subtracted with rolling paraboloid and a 5-pixel rolling ball radius in Fiji 1.54j.[33] This was done using the GFP channel only, as it showed a stronger signal. Afterwards, the images were analyzed using a modified CellProfiler 4.2.6[34] pipeline previously established by a former master project. (**Fig 5**) First, the images were stretched to their full intensity range ("RescaleIntensity"), after which they were identified based on the upper and lower bound of their pixel diameter ("IdentifyPrimaryObjects"). Next, their diameter and shape were measured ("MeasureObjectSizeShape"). Any clumped droplets or non-droplet objects were filtered out ("FilterObjects") and size and shape were measured again

14

Materials and Methods

("MeasureObjectSizeShape"). From the filtered droplets, intensity and intensity distribution were measured. ("MeasureObjectIntensity" and "MeasureObjectIntensityDistribution"). To verify the correct execution of the pipeline, a test image was created every cycle that overlayed the base image, the identified objects and the filtered objects. (2x "OverlayObjects", "Tile", "Resize"). To calculate results, the pixel area per droplet was used to calculate the diameter. For homogeneity, the standard

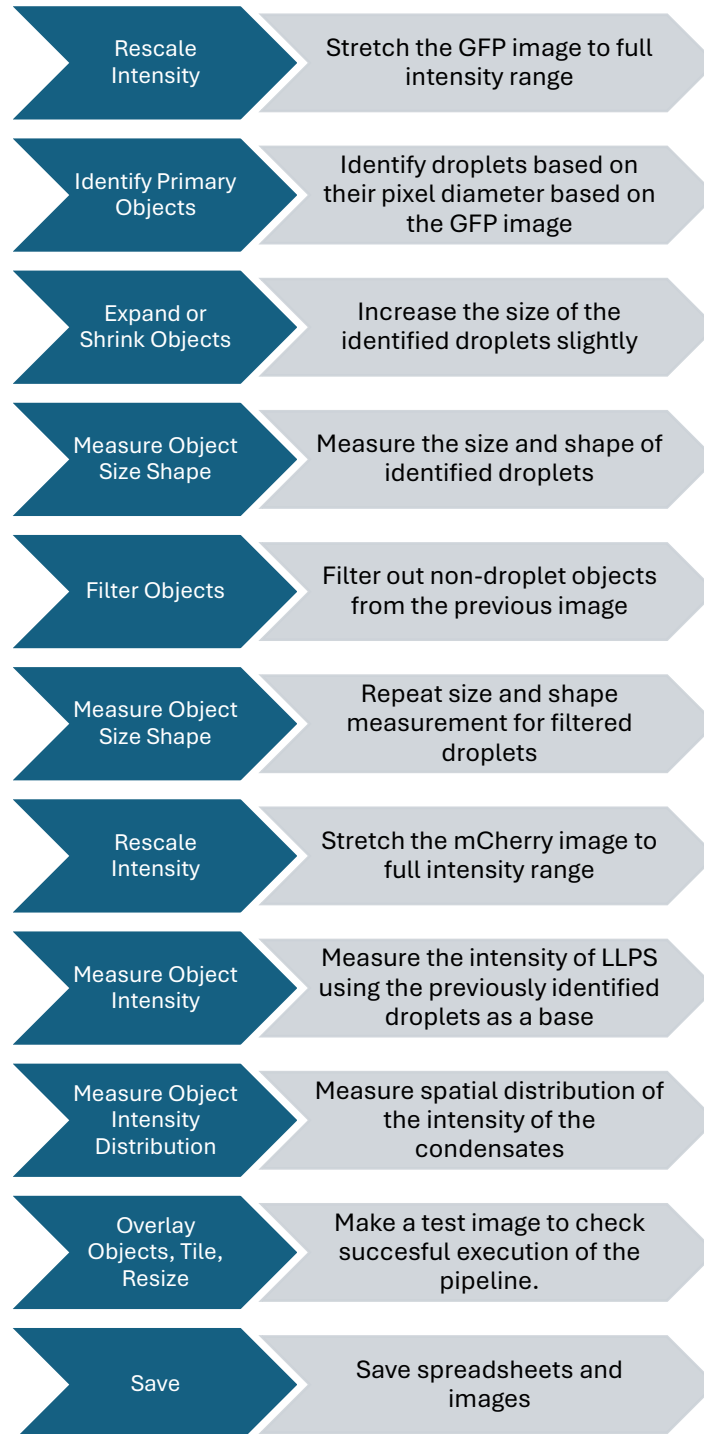|	
Rescale Intensity	Stretch the GFP image to full intensity range
Identify Primary Objects	Identify droplets based on their pixel diameter based on the GFP image
Expand or Shrink Objects	Increase the size of the identified droplets slightly
Measure Object Size Shape	Measure the size and shape of identified droplets
Filter Objects	Filter out non-droplet objects from the previous image
Measure Object Size Shape	Repeat size and shape measurement for filtered droplets
Rescale Intensity	Stretch the mCherry image to full intensity range
Measure Object Intensity	Measure the intensity of LLPS using the previously identified droplets as a base
Measure Object Intensity Distribution	Measure spatial distribution of the intensity of the condensates
Overlay Objects, Tile, Resize	Make a test image to check succesful execution of the pipeline.
Save	Save spreadsheets and images

Figure 6: Flowchart showing the chronological order of the CellProfiler Pipeline modules used for measuring the LLPS in the glass capillaries.

deviation of pixel intensity per droplet was used. A similar approach was made for droplet velocity calculations. The images were prepared the same way as before. The CellProfiler Pipeline stretched the images to their full intensity range ("RescaleIntensity"), and the droplets were again identified by the upper and lower bounds of their pixel diameter ("IdentifyPrimaryObjects"). Next, the droplet`s size and shape were measured ("MeasureObjectSizeShape") and any clumped or non-droplet objects were filtered out ("FilterObjects"), with the size and shape of the filtered image being measured again ("MeasureObjectSizeShape"). Next, the objects were tracked ("TrackObjects") based on the pixel distance from one image to another. This distance was 20 pixels for the 135 Hz chips, while 50 pixels were used for the 235 Hz chips. A minimum lifetime of 10 frames was also chosen, meaning a tracked droplet had to appear on 10 images to be considered. Each cycle was also accompanied by a verification image that showed the original image and the tracked droplets. ("OverlayOutlines", "Tile") To interpret the results, the X-axis displacement of each frame was used to indicate movement, meaning the pixel distance in the x direction of a tracked droplet between two frames. Using the known pixel-to-length ratio and the known 100 ms gap between each image, the average velocity was calculated and visualized in a histogram.

For the capillary LLPS experiments, the images were again prepared using ImageJ Fiji 1.54j. For the GFP images, a Z-stack projection was made, using the average of all z images, while the mCherry protein images were Z-stacked using the standard deviation of all images. This was done because an average of all Z-stacks would have erased the fluorescent Dhh1 condensates, while Z-projection by standard deviation would have highlighted them. Afterwards the "subtract background" tool was applied using the sliding paraboloid option and a 5-pixel rolling ball radius. Both image stacks were then extracted using the Bio-Formats plugin, so each image was individually named and ready for CellProfiler (**Fig 6**). First, the GFP images were stretched to their full intensity range ("RescaleIntensity"), after which the droplets were identified based on the upper and lower bounds of their pixel diameter ("IdentifyPrimaryObjects"). The identified droplets were expanded by 20 pixels ("ExpandOrShrinkObjects") to account for the high amount of LLPS speckles found in the droplet border regions. These identified droplets were measured for size and shape ("MeasureObjectSizeShape"). Next, the mCherry images were stretched to their full intensity range ("RescaleIntensity"). The Intensity and intensity distribution were measured ("MeasureObjectIntensity" and "MeasureObjectIntensityDistribution"), using the previously identified and expanded GFP droplets as a base, since the GFP channel image had a sharper and stronger signal.

Materials and Methods

To verify, test images showing the original image, the identified primary objects and the filtered objects were overlaid and saved for each image (2x "OverlayObjects", "Tile", "Resize"). To measure the amount of LLPS, the standard deviation of each droplet was taken as a measure for the amount and size of speckles and plotted in OriginPro 2023b.

Protein Expression and Purification

The monomeric Dhh1 was expressed in New England Biolabs® Lemo21(DE3) competent E .coli (C2528J) bacteria. 50 µl of bacteria, thawed on ice, was mixed with 2 µl of plasmid. After slight shaking, the bacteria-plasmid mixture was left on ice for 10 minutes, after it was subjected to heat shock for 1 minute in a 42°C water bath. Following 5 minutes of regeneration on ice, the bacteria were added to a 250 ml Erlenmeyer flask containing 50 ml of lysogeny broth (LB) containing Ampicillin (AMP). Additionally, Chloramphenicol (CAM) and 1% Glycose were added to the growth medium. This culture was grown overnight in a shaker incubator at 200 rpm at 30°C. The next day, a large culture was prepared in a 5 l Erlenmeyer flask. The mixture contained 100 ml 1M pH 7.5 phosphate buffer, 1 ml 1000x (34 mg/mL) Chloramphenicol, 1 ml 1000x Ampicillin (50 mg/mL) and 900 ml of terrific broth (TB). After measuring the optical density (OD) of the starter culture at 600 nm, the growth in the main culture was started at an OD of 0.025. At 37°C and 100 rpm, this culture was grown until an OD of 0.6 – 0.7 was reached, after which it was induced with 300 µM Isopropyl β-D-1-thiogalactopyranoside (IPTG). Afterwards, it was grown overnight at 18°C with 110 rpm. Following, the resulting culture was filled in 500 ml bottles and spun down for 15 minutes at 5000 rpm. The bacterial pellet was removed and the supernatant discarded. The pellet could now be frozen at -80 °C for storage or used immediately.

The pellet was then mixed with a binding buffer (consisting of 58.44 g / 200 mL NaCl 5 M Stock solution, 50 mL Tris pH = 8.0 (1 M), 126 g / 100 mL Glycerol, 25 mM Imidazole and filled up to 1 L with Milli-Q water) under constant stirring for 30 minutes. Further, 1:200 DNAse, 1:200 RNase and 1:500 protease inhibitors were added. The lysis process was done in an Emulsiflex machine. The cycle ran a few times until slight foaming indicated a successful lysis. The lysate was further sonicated for 10 minutes at 4 °C. The lysate was filled into 45 mL centrifugation tubes and spun down at 4 °C at 80000 g for 90 minutes. Immobilized Metal Affinity Chromatography (IMAC) was performed on the cytiva™ Äkta pure™ chromatography system. Buffer A consisted of the binding buffer, Buffer B of binding buffer plus 500 mM Imidazole. A gradient elution from 5% to 100% was used. The purified protein was fractionated into a well plate. The wells used for further purification were determined using a sodium dodecyl sulfate–polyacrylamide gel electrophoresis

Materials and Methods

(SDS-PAGE) assay. 3C protease was used to cleave the Histidine tag of the filtered protein. The protein was filled into a Spectra/Por® 12-14 kDa dialysis membrane and left overnight in dialysis buffer (consisting of 58.44 g / 200 mL NaCl 5 m Stock solution, 50 mL Tris pH = 7.5 (1 M), 126 g / 100 mL Glycerol, 25 mM Imidazole, Filled up to 1 L with Milli-Q water, 206 µl of 2-Mercaptoethanol (14.5 M) and 2 mM $MgCl_2$). To get rid of any uncleaved protein, the protein solution was run through the chromatography system in a reverse IMAC, using the dialysis buffer. The protein solution was then concentrated in an Amicon® 30kDa MWCO filter tube at 4000 g. The protein was further filtered in a 0.2 µm cellulose acetate filter and taken up in a syringe for injection into the cytiva™ Äkta pure™ loop. In the final purification step, the protein was run through a HiLoad™ 16/600 Superdex™ 200 pg sizte exclusion column for size exclusion chromatography (SEC) using a size exclusion buffer (consisting of 58.44 g / 200 mL NaCl 5 m Stock solution, 50 mL Phosphate pH = 7.5 (1 M), 126 g / 100 mL Glycerol, filled up to 1 L with Milli-Q water, 206 µl of 2-Mercaptoethanol (14.5 M) and 2 mM MgCl2) and fractionated into a well plate. To check for successful size exclusion, an SDS-PAGE was done. The chosen wells were further concentrated using Amicon® 30 kDA MWCO filters until a protein concentration of at least 200 µM was reached.

Results and discussion

Classical LLPS Assays

First, we sought to confirm the role of RNA on phase separation. Proteins pMH1674, pMH1930 and pMH1931 were combined with a master mix at concentrations ranging from 18 μM to 3.8 μM. Without added RNA, no LLPS was visible (**Fig. 7a**). However, with RNA added, clear LLPS was now visible for the pMH1674 variant, but not for pMH1930 and pMH1931 (**Fig. 7b**). The assay with the PolyU containing master mix was repeated to confirm the result. As the pMH1930 and pMH1931 mutations are unable to bind RNA, the theoretical importance of RNA binding for LLPS was strengthened. Based on these results, further LLPS experimentation using RNA was planned, with a minimal protein concentration of 5 μM. To determine the ideal conditions for the LLPS trigger solution, a DoE was created, using the OriginPro™ Design of Experiment application[35]. Tested conditions were pH level (pH = 6.4 and pH = 7.2), concentration of NaCl (100 mM and 200 mM), addition of ATP (no ATP or 2 mM ATP) and the addition of PolyU (no PolyU or 0.05 mg/ml PolyU). Each well contained Dhh1- K234D-V238D (pMH1806) concentrated at 5 μM. The final mixtures (**Appendix Table 1**) were visualized in a 96-well plate using a Nikon™ Eclipse Ti2-E™ Inverted Research Microscope at 25°C. A strong LLPS was visible for the mixtures containing 0.05 mg/ml polyU at a pH of 6.4 (**Fig. 7c**). The results underscored the importance of RNA and pH level for LLPS, while salt concentration and ATP were less influential. Subsequently, the trigger solution for LLPS experiments contained a fixed amount of 0.05 mg/ml PolyU at a pH = 6.4. ATP was omitted. Since the salt concentration is known to influence LLPS, further experiments explored the relationship between NaCl concentration and LLPS more than the simple two-factor design used in the presented DoE experiment.

Chip Design

The first iteration of the chip design was based on the design used by *Linsenmeier et al.*, 2019[36] (**Fig. 8a**). In this initial design, the inlets for the solutions used in the experiment were lined up sequentially, one after another. The droplets at the generating junction were then pushed into a delay structure that terminated into an outlet, where droplets could be disposed into a waste receptacle or used for further off-chip analysis. Due to the phase separation of the Dhh1 protein, droplet generation experiments were forced to use combined flow rates of up to 5 μl/min in order to keep the channels free of protein accumulations. At these flow rates, the droplets were too

19
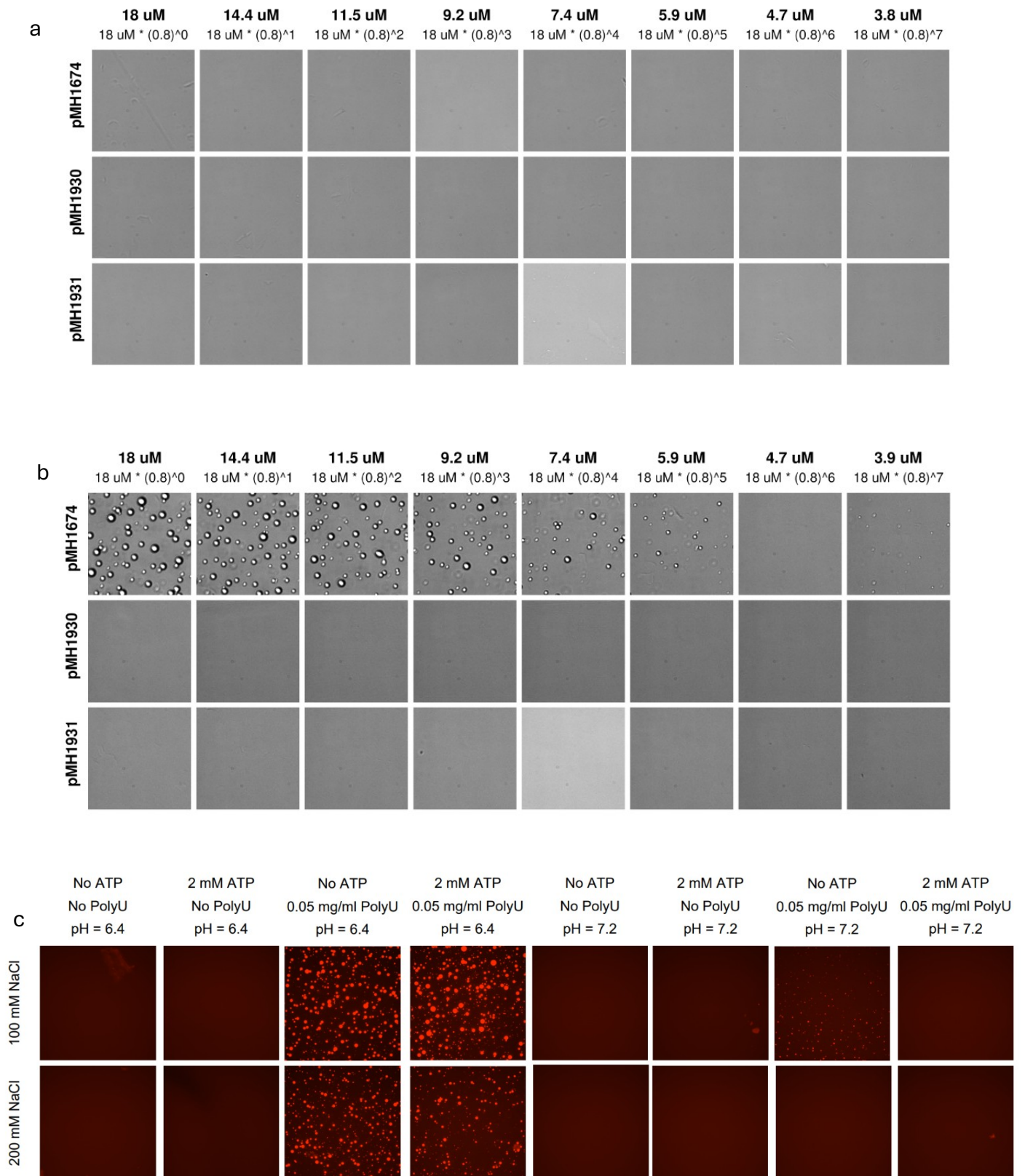
Results and Discussion

Figure 7: ***a.*** *The LLPS assay of the Dhh1 mutations and their corresponding concentrations. No PolyU was added in this assay.* ***b.*** *The LLPS assay of the Dhh1 mutations and their corresponding concentrations. PolyU was added in this assay.* ***c.*** *The DoE assay showing the different conditions under which the Dhh1-K234D-V238D protein undergoes LLPS.*
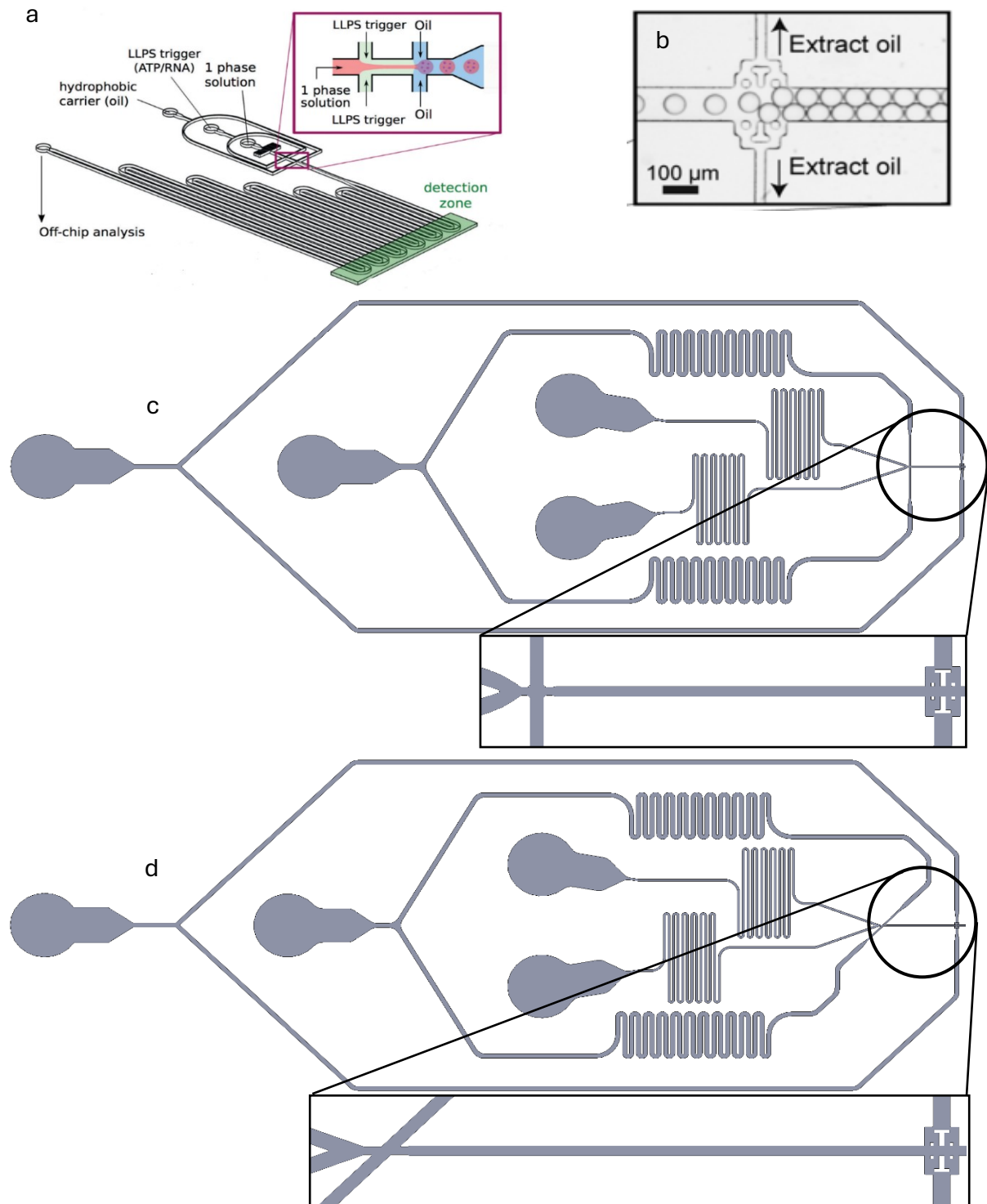
Results and Discussion

Figure 8: *a*. *The initially used chip design showing the inlets for the oil, LLPS trigger and 1-phase (protein) solutions. Further, the delay structure and the outlet for the droplets are shown. Illustration adapted from Linsenmeier et al., 2019. **b**. The oil extraction element, which diverts the flow of the oil phase to the side and allows a slower, controlled flow of the droplets. Illustration adapted from Frenz et al., 2009. **c**. The symmetric chip design, including details of the droplet generator and the oil extractor (Delay elements not pictured). **d**. The asymmetric chip design, including details of the droplet generator and the oil extractor (Delay elements not pictured).*

fast to be imaged by the Eclipse Ti2-E™. Since on-chip imaging was not feasible with the initial design, a simplified version of the chip was created, which removed the delay

structures. This design was used for off-chip analysis of droplets filled with phase-separating protein.

After initial experiments on droplet generation and LLPS in droplets, building on the previously established chip design, new designs were required in order to go from capillary imaging to on-chip imaging on the microfluidic chips. The chips were thus completely redesigned, for which various alternate designs were considered. Based on a design by *Frenz et al.*[37] (**Fig. 8b**), an oil extraction line was introduced after the droplet-generating nozzle. By allowing the oil phase to flow out after droplets have been generated, the droplets enter the subsequent channel with a much lower velocity and thus allow for easier analysis. An additional delay element was introduced before the

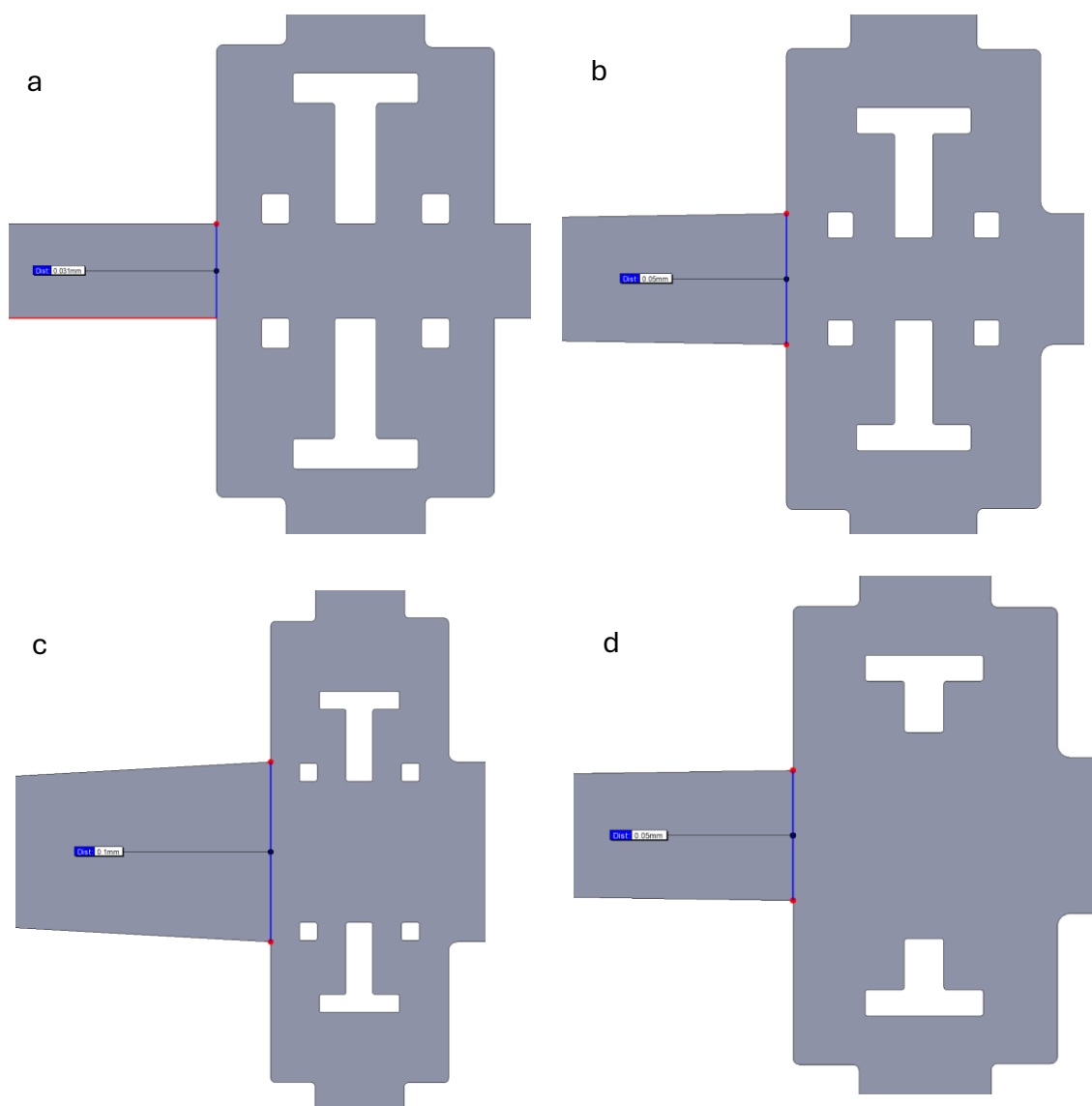*Figure 9: The 4 iterations of the oil extraction element. **a**. The first iteration with the design close to the one used by Frenz et al. **b**. and **c**. The next iteration with a funnelled droplet generator outlet and a more spacious oil extractor. The outlets were the size of 50 µm and 100 µm, respectively. **d**. The final outlet design with a more simplified and shortened design. The outlet was the size of 60 µm.*

droplets exited the outlet. The droplet generator was also completely redesigned, with the trigger and protein phases meeting at a junction flanked by two oil channels. Further delay structures were also introduced to the oil, trigger and protein channels in order to achieve a more continuous flow and allow more reaction time to any irregularities in the flow behavior. Two versions of the droplet generator were created, with one symmetric (**Fig. 8c**) and one asymmetric (**Fig. 8d**). The asymmetric structure was theorized to aid the mixing of the phases and thus produce more homogeneous droplets, based on the paper by *Belousov et al.*[38] The dimensions of the droplet generator were based on DAFD.[39] DAFD is a machine-learning based model that uses geometric parameters and flow rates to predict droplet generation rate (Hz) and droplet diameter (μm). Chips with generation rates of 135 Hz, 235 Hz, 500 Hz and 1000 Hz were produced. Their exact measurements and predicted attributes can be found in **Appendix Table 2**. Due to issues with droplets getting stuck in the initial oil extractor design (**Fig. 9a**), a first revision made the outlet channel funnel into the oil extractor, with the square stabilizing elements in the oil extractor being pushed more towards the outlets to prevent droplets from getting stuck. This issue saw improvement after the widening of the funnel and the extractor element (**Fig. 9b and 9c**), but was not fully eliminated. Another factor was the thickness of the final delay structure, with a 50 μm and a 100 μm version being produced. In the 50 μm version, droplets that entered the final delay structure showed inconsistent velocity. This was due to increasing pressure in the delay channels from droplets clogging up the outlet. At a certain point, the droplet flow stopped completely. Newly generated droplets were now squeezed together in the delay channels until they became square or even completely liquefied. The majority of the generated droplets however were flushed out through the oil extraction channel, as the resistance in this channel was much lower. The 100 μm version suffered similar flow issues, additionally also showing multiple droplets entering the channel at the same time. Another revision was made in order to address these issues. The oil extraction element was further simplified by removing the square elements and shortening the T-shape elements. (**Fig. 9d**) It was decided to make the delay channel 60 μm, to allow for more flow while preventing more than a single droplet from entering the delay elements. It was also assumed that the length of the delay elements was a cause for the slowing of the droplets, and thus the length of the delay elements was reduced.

Droplet attributes and capillary imaging of LLPS
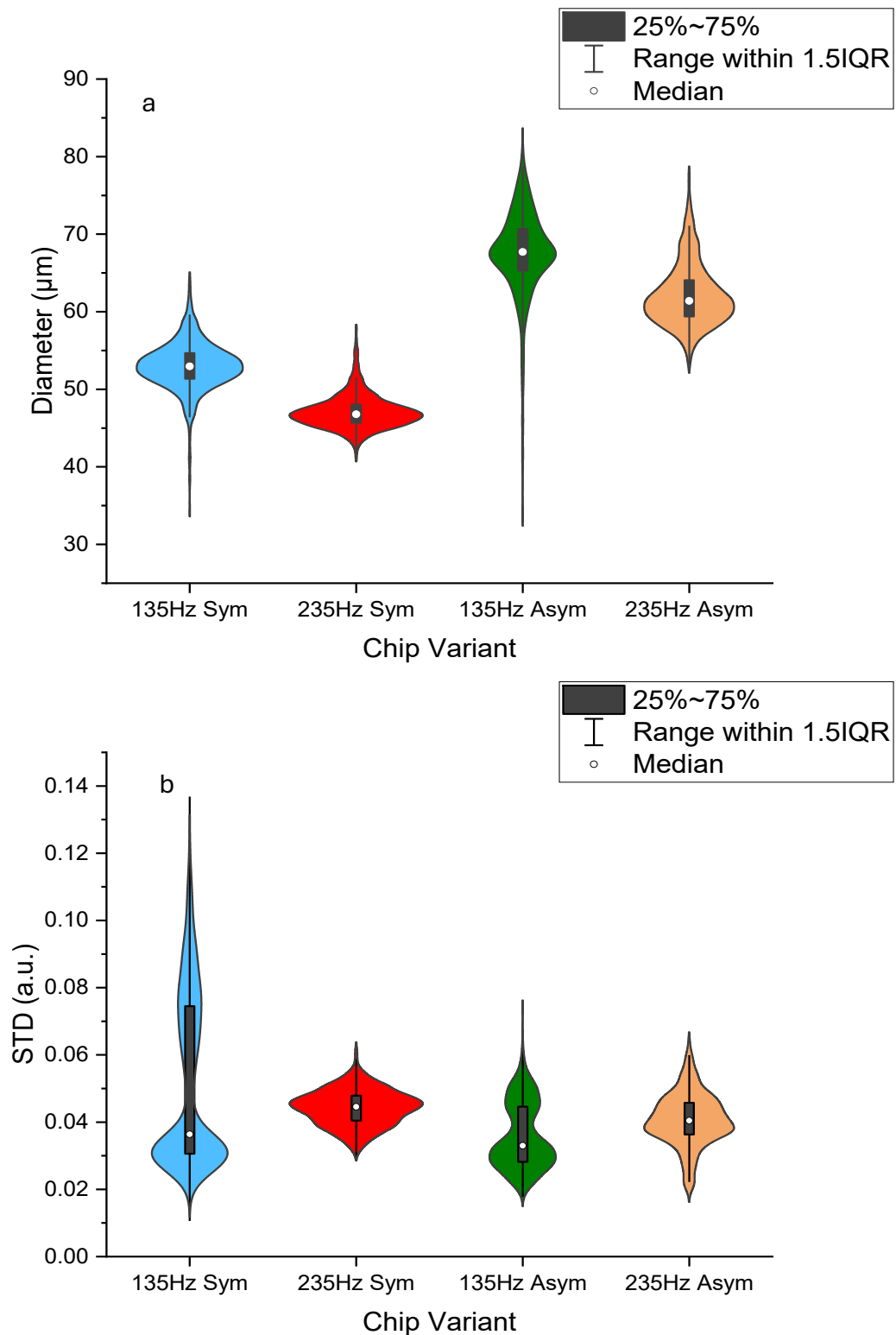
*Figure 10: **a**. The average diameter of the generated droplets of all tested chip variants. **b**. The average standard deviation of the intensity of the generated droplets in all tested chip variants.*

First, the theoretical attributes of the droplets established by DAFD were tested in a droplet generation experiment using the redesigned chips shown in **Figure 8**, but with a straight outlet (thickness = 1 mm) after the oil extractor (**Fig. 11**). As conditions to

establish reliable and repeatable on-chip analysis of LLPS were not worked out at this point of the project, this simplified version was chosen to avoid issues with solution flow. Further, the trigger solution was substituted for a fluorescein mix and the protein was substituted with a rhodamine solution. After a short flush of the chip with oil, all syringe pumps were turned on (Refer to **Appendix Table 2** for flow rates). After a stable flow of oil
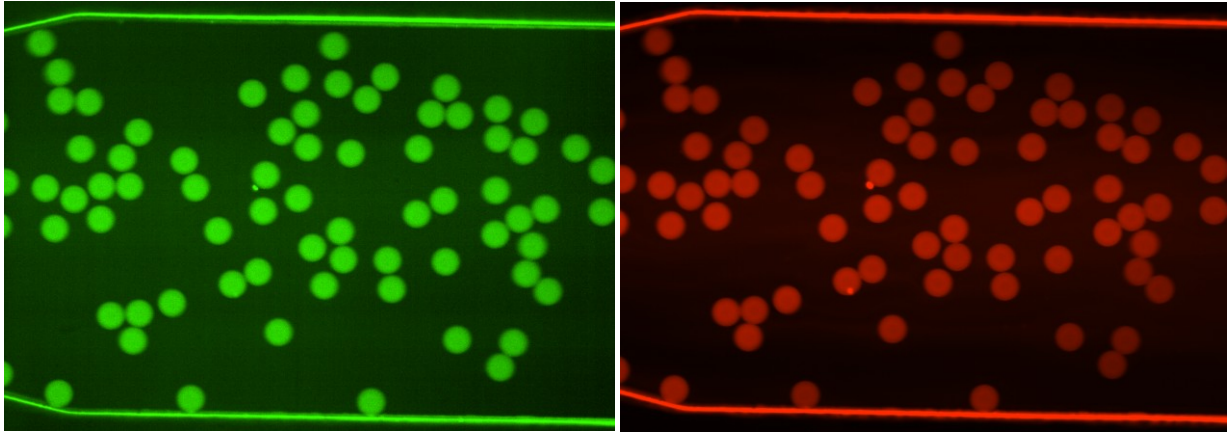

Figure 11: An example comparison of a 135 Hz chip with an asymmetric droplet generator showing the droplets in the 1 mm outlet channel, with both the fluorescein dye (right) and the rhodamine dye (left) visible.

and fluorescent solution at the inlet junction was established, the outlet channel was imaged. Image sets for the analysis of diameter, homogeneity and velocity were made.

Chips with a predicted generation rate of 135 Hz and 235 Hz were tested, with a symmetric and asymmetric droplet generation junction. Each condition was tested in triplicate. The results are shown in **Figure 10**. The average droplet diameter of the symmetric 135 Hz chips was 53±3 µm, while the asymmetric 135 Hz chips showed a larger average droplet diameter of 68±6 µm. The symmetric 235 Hz chips showed an average diameter of 47±2 µm, while their asymmetric 235 Hz counterpart had an average diameter of 63±4 µm (**Fig. 10a**). This showed a significant difference between the predicted droplet size and the actual droplet size. The droplets in the asymmetric chips were found to be larger than in the symmetric chips. In the case of the 135 Hz chips, the asymmetric chips produced droplets 15 µm larger than the symmetric ones. Similarly, the 235 Hz chips showed a 16 µm increase in size, going from symmetric to asymmetric. This highlights the limitations of the prediction model, as the model only takes purely mechanical factors into account. However, the prediction still served as a useful starting point for further experimentation and allowed one to go from initial design to practical application faster. Previously it was theorized that chips with an asymmetric droplet generator would lead to more homogenous droplets. To assess whether this is true, the same droplets imaged for their average diameter were analyzed for the standard deviation (STD) of their pixel values. The results showed an average pixel STD for the symmetric 135 Hz chip of 0.05±0.03, while

the asymmetric 135 Hz variant showed a mean STD of 0.04±0.01. For the symmetric 235 Hz chip variants the mean STD was 0.04±0.006, while the asymmetric 235 Hz chip showed a mean STD of 0.04±0.008 (**Fig. 10b**). Thus, no clear difference in homogeneity emerged. The impact of the asymmetric droplet generator on droplet mixing was not confirmed and due to time constraints, it was decided to conduct subsequent experiments with the symmetric variants of the microfluidic chips only. The final result from the fluorescent dye experiment was the average velocity of the droplets. The 135 Hz symmetric chip showed an average velocity of 335 µm/s, while the asymmetric variant showed an average of 356 µm/s. The symmetric 235 Hz chip showed an average velocity of 386 µm/s, the asymmetric variant 444 µm/s. The histogram (**Fig. 12**) showed a more Gaussian distribution for the 135 Hz chip variants. The 235 Hz chips meanwhile had a more flattened velocity distribution, while also showing a significant amount of negative displacement values, which would correspond to movement in the opposite direction. All negative values were suppressed before plotting. The most probable cause for this issue is the CellProfiler pipeline. The increased speed and density of the droplets in the higher frequency 235 Hz chip variants made it more difficult for the module to identify correlated droplets between one frame and the next. The same issue also caused the negative displacement values, as the program misidentified different droplets belonging together.
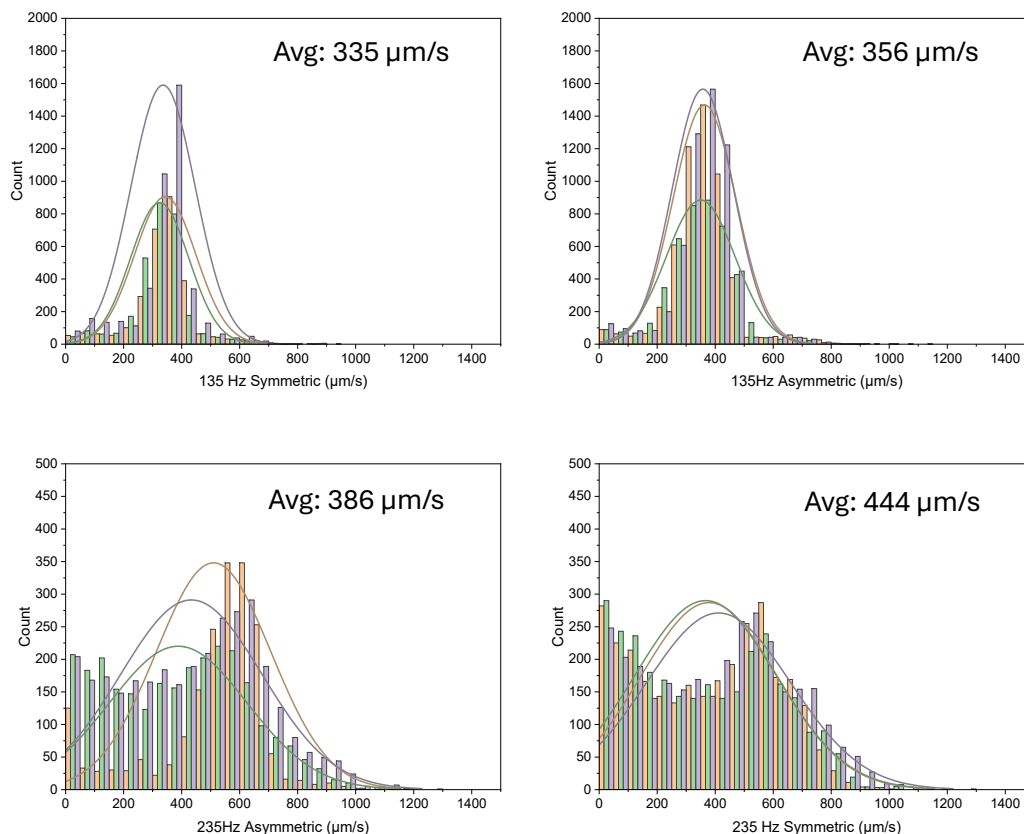

Figure 12: Histograms representing the droplet velocity in different chip variants. The orange, purple and green bars represent one replicate each.
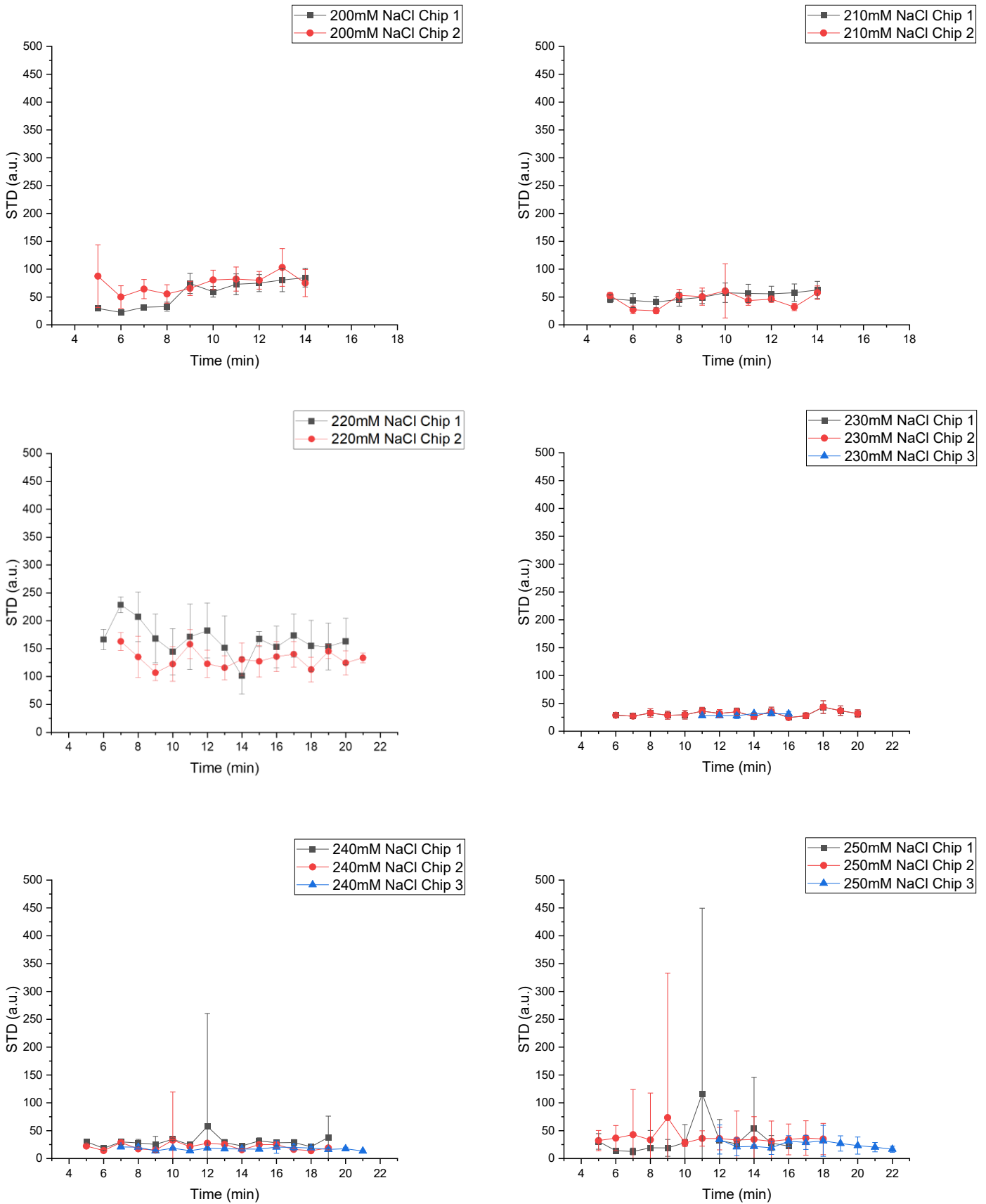
Results and Discussion

Figure 13: The standard deviation of the intensity of droplets for each chip variant.

Results and Discussion

Next, while preparing the system for live imaging, we tried to image time-dependent LLPS droplet formation using glass capillaries. Since the influence of salt concentration was previously established as an important factor for droplet formation, different concentrations were imaged to assess whether the formation kinetics would be markedly influenced. As described in the method section, 10 different positions for the 200mM and the 210mM NaCl samples were picked, while 15 positions were picked for the 220mM, 230mM, 240mM and 250mM NaCl samples. However, after analysis, no clear formation kinetics pattern emerged. Overall, the average phase separation stayed remarkably consistent over the course of the image time series, which indicates most of the formation takes place before the imaging. (**Fig. 13**) This indicated a flaw in the method, as the time of transferring the capillary containing the droplets to the microscope for imaging never went below 5 minutes, which was possibly a critical timeframe for droplet formation.

Final Chip design and live imaging

In order to achieve live imaging that combines visualization of droplet attributes and LLPS in a live system, major flaws in the chips had to be corrected. Experience with previous experiments showed that even with Trichloro(1H,1H,2H,2H perfluorooctyl) silane treatment there were still accumulations of protein clumps in critical parts of the chip, such as the oil extraction junction. BSA was used in an attempt to both address the protein accumulation and support a continuous droplet flow in the delay structures. However, flushing with BSA showed similar issues as with the droplet experiment, with the flow coming to a halt inside the delay structure. The original idea of a 30 µl/h flow
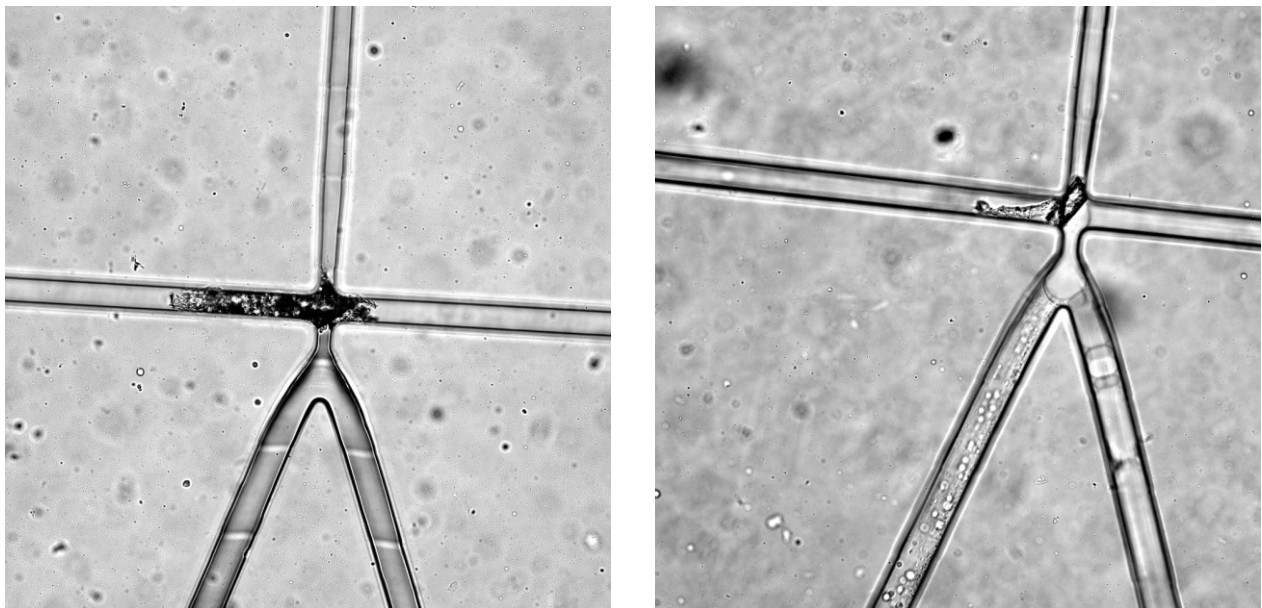

Figure 14: Examples of channel obstructions encountered during live-imaging experiment after BSA flushing.

Results and Discussion

overnight was abandoned as non-feasible. The chips were flushed with 200 µl/h for 15 minutes, from both the oil inlet and the droplet outlet to ensure all channels being saturated with BSA. The oil outlet was plugged by a piece of copper wire to increase flow pressure. Starting with the new chip designs, previously unnoticed particles were spotted in the inlets and channels (**Fig. 14**). Once a flow was applied, these particles would accumulate in critical parts of the chip, such as the droplet generator or oil extractor. It was theorized that drying out of the BSA used for flushing and channel saturation could cause flaking. To remedy the issue, the chip outlets were flushed with water immediately after application of BSA, and then covered with another droplet of water to prevent drying out. However, particles still persisted. Testing chips that were not prepared with BSA also showed present particles. The issue was reduced by first sonicating the chips in Isopropyl alcohol, then drying them out using pressurized N_2. They were dried further at 95 °C for 15 minutes, after which they were immediately flushed with BSA into the final outlet, while the oil outlet was plugged. After 15 minutes, the flow was stopped and experiments were begun immediately to prevent drying out. Simultaneously, previously described flow velocity issues were also still present. A temporary solution was found by turning on a high oil flow of up to 500 µl/h while keeping the oil outlet plugged by a copper wire. After a uniform flow was achieved, the oil outlet plug was removed and the oil flow rate slowly reduced to the level determined by DAFD. At the same time, the flow of the trigger and protein solutions was turned back on, which allowed droplet generation for a few minutes before slowing down and stopping again. While the droplets initially flowed rather consistently (**Fig 15a and 15b**) and showed a rounded appearance, after a few minutes the flow would decline and droplets at the front of the flow would begin to lose their
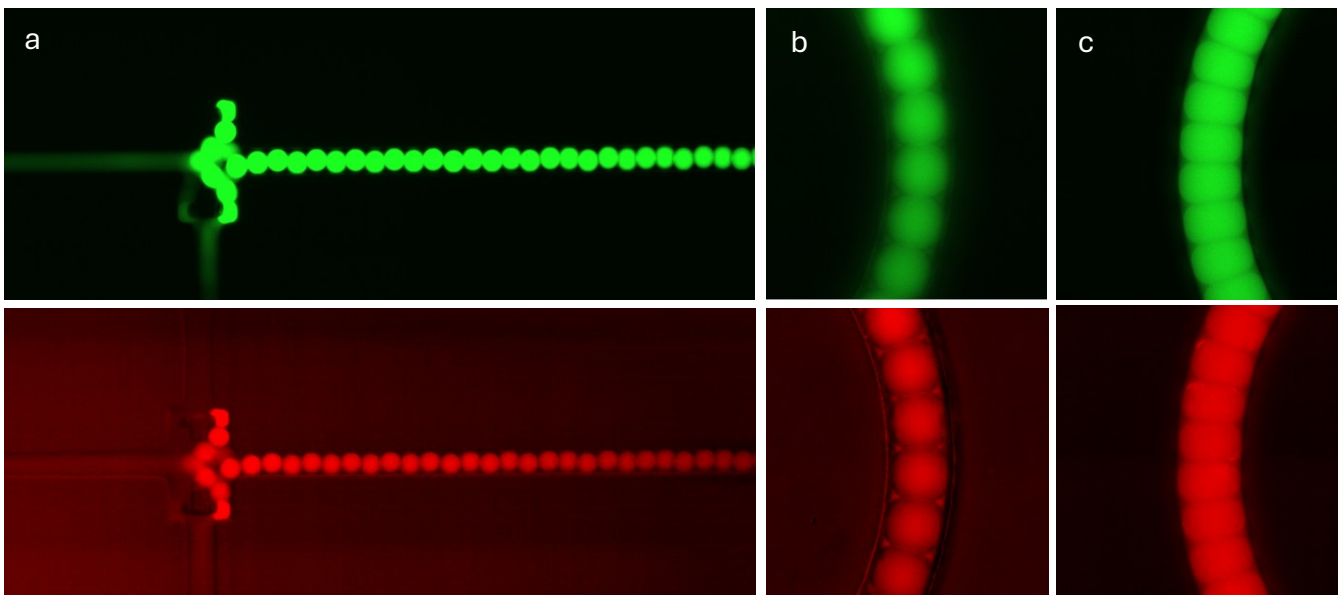
Figure 15: *a*. *Images of the droplet generator in the GFP (green, trigger solution) and mCherry (red, protein) channels.* *b*. *Images of the first bend in the delay structure showing round droplets.* *c*. *Images of the 7th bend of the delay structure showing more square droplets.*

original shape. They would become squished and, in some cases, even completely dissolve due to pressure. The lack of flow motivated a final rework of the chip, with three versions with reduced delay structure length.

Conclusion and Outlook

This thesis represented an attempt at creating a microfluidics system able to easily create phase-separated protein-containing droplets and allow their study. This system represented numerous advantages over typical LLPS assays, such as natural fluid mixing and immediate imaging after droplet generation. Further, we wanted to introduce RNA as a factor in order to further develop an understanding of RNA-RNA interactions for phase separation. However, the design and functionalization of the PDMS microfluidic chip turned out to be major challenges with numerous problems that had to be overcome. Significant time was spent on redesigning the chip to address mechanical flow issues. Similarly, issues with forces such as adherence of protein to non-functionalized channels were also occurring. The ever-increasing quantity of microfluidic papers and other scientific output however ensured that solutions could be found by relying on other groups working with microfluidics. Other problems remained unsolved as of the end of the project, however. The particles that were present during the live imaging experiments persisted and no long-term solution was found. Future chip designs could include filter elements on the inlets to prevent the particles from entering critical parts of the chip. To address issues with the droplet flow, a slimmed- down outlet was conceptualized, where the reduced width of the outlet would allow easier droplet outflow. This way, there would be less pressure build-up in the delay channels and the successful flow would continue for longer. Besides the final design, experimental chips (**Fig. 16**) were designed based on
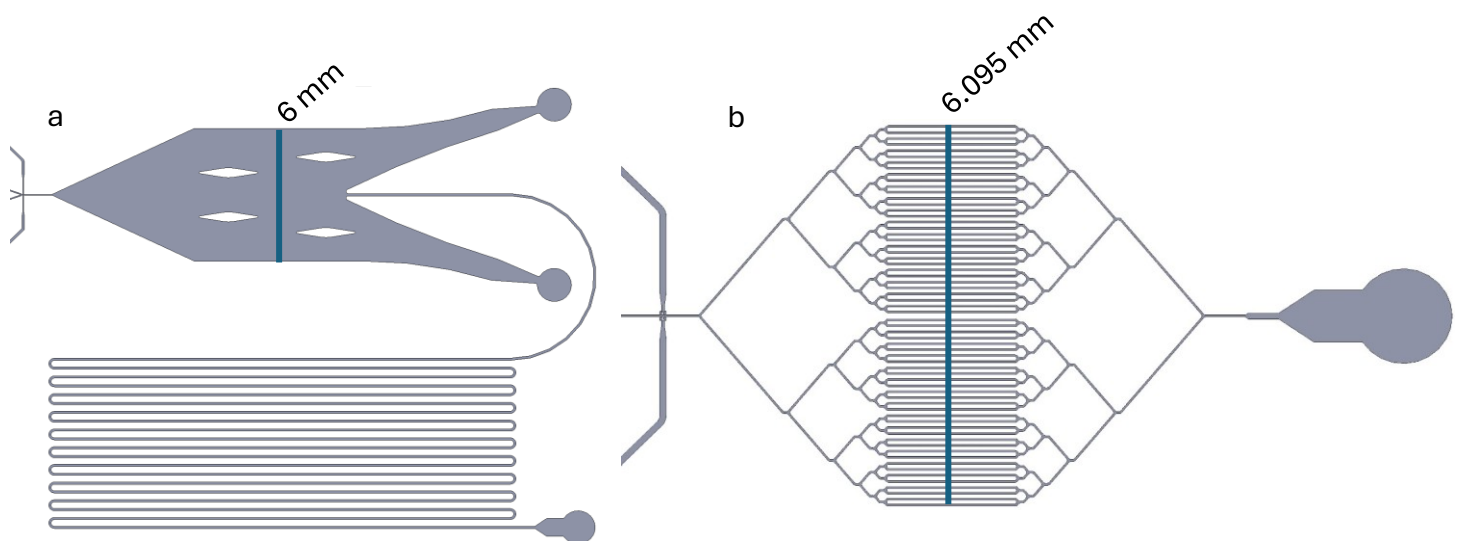

*Figure 16: **a**. The design „Blooper" with a large reservoir that would have allowed droplets to accumulate and slowly enter the exit channels. Based on a design by Courtois et al., 2018 **b**. The design "Yggdrasill" where droplets would be slowed by increasingly branched-out delay channels.*

other literature that were not used, as it was decided to dedicate our main efforts to one design. These design properties would have differed substantially from the chip used and it is thus hard to predict how they would have influenced the final results. If additional syringe pumps were available, an extra inlet could have simplified experiments that required a single parameter change. For example, to vary NaCl levels, the trigger solution had to be discarded, the syringe cleaned and a new trigger solution mixed. This not only wasted material and time, but also reduced consistency, as slight variations in trigger solution mixing were unavoidable. With an additional inlet, a NaCl-containing solution could have been inserted into the flow of the trigger solution before the droplet generator. This could have been applied to PolyU and ATP solutions as well.

Overall, with a substantial amount of the allotted time being spent on improving chip design, working out a more elaborate theoretical framework before starting with the practical work could have potentially saved time spent on trial-and-error. Due to this, the scope of the project exceeded the intended 6 months, and the question of RNA-RNA interaction influence on LLPS could not be answered. However, the project still succeeded in substantially expanding the theoretical and practical knowledge of our microfluidic setup and thus could pave the way for a future project to continue and expand investigation into LLPS.

Acknowledgements

Bibliography

1. Diekmann, Y. & Pereira-Leal, J. B. Evolution of intracellular compartmentalization. *Biochem. J.* **449**, 319–331 (2013).

2. Harold, F. M. Molecules into Cells: Specifying Spatial Architecture. *Microbiol. Mol. Biol. Rev.* **69**, 544–564 (2005).

3. Howard, M. How to build a robust intracellular concentration gradient. *Trends Cell Biol.* **22**, 311–317 (2012).

4. Caudron, F. & Barral, Y. Septins and the Lateral Compartmentalization of Eukaryotic Membranes. *Dev. Cell* **16**, 493–506 (2009).

5. Ovádi, J. & Saks, V. On the origin of intracellular compartmentation and organized metabolic systems. *Mol. Cell. Biochem.* **256**, 5–12 (2004).

6. Pederson, T. The Nucleolus. *Cold Spring Harb. Perspect. Biol.* **3,** a000638–a000638 (2011).

7. Taliansky, M. E., Love, A. J., Kołowerzo-Lubnau, A. & Smoliński, D. J. Cajal bodies: Evolutionarily conserved nuclear biomolecular condensates with properties unique to plants. *Plant Cell* **35**, 3214–3235 (2023).

8. Ilık, İ. A. & Aktaş, T. Nuclear speckles: dynamic hubs of gene expression regulation. *FEBS J.* **289**, 7234–7245 (2022).

9. Wang, Y. & Chen, L.-L. Organization and function of paraspeckles. *Essays Biochem.* **64**, 875–882 (2020).

10. Patra, U. & Müller, S. A Tale of Usurpation and Subversion: SUMO-Dependent Integrity of Promyelocytic Leukemia Nuclear Bodies at the Crossroad of Infection and Immunity. *Front. Cell Dev. Biol.* **9,** 696234 (2021).

Bibliography

11.   Biamonti, G. & Vourc'h, C. Nuclear Stress Bodies. *Cold Spring Harb. Perspect.*

        Biol. **2**, a000695–a000695 (2010).

12.   Kulkarni, M., Ozgur, S. & Stoecklin, G. On track with P-bodies. *Biochem. Soc.*

        Trans. **38**, 242–251 (2010).

13.   Protter, D. S. W. & Parker, R. Principles and Properties of Stress Granules. *Trends*

        Cell Biol. **26**, 668–679 (2016).

14.   Mugler, C. F. *et al.* ATPase activity of the DEAD-box protein Dhh1 controls

        processing body formation. *eLife* **5**, e18746 (2016).

15.   Linder, P. & Jankowsky, E. From unwinding to clamping — the DEAD box RNA

        helicase family. *Nat. Rev. Mol. Cell Biol.* **12**, 505–516 (2011).

16.   Hondele, M. *et al.* DEAD-box ATPases are global regulators of phase-separated

        organelles. *Nature* **573**, 144–148 (2019).

17.   Strahl-Bolsinger, S. & Tanner, W. A yeast gene encoding a putative RNA helicase of

        the 'DEAD'-box family. *Yeast Chichester Engl.* **9**, 429–432 (1993).

18.   Stevens, A. mRNA-Decapping Enzyme from *Saccharomyces cerevisiae* :

        Purification and Unique Specificity for Long RNA Chains. *Mol. Cell. Biol.* **8**, 2005–2010

        (1988).

19.   Barbee, S. A. *et al.* Staufen- and FMRP-Containing Neuronal RNPs Are

        Structurally and Functionally Related to Somatic P Bodies. *Neuron* **52**, 997–1009

        (2006).

20.   Cheng, Z., Coller, J., Parker, R. & Song, H. Crystal structure and functional

        analysis of DEAD-box protein Dhh1p. *RNA* **11**, 1258–1270 (2005).

Bibliography

21. Linsenmeier, M. *et al*. Dynamic arrest and aging of biomolecular condensates are modulated by low-complexity domains, RNA and biochemical activity. *Nat. Commun.* **13**, 3030 (2022).

22. Cascarina, S. M. & Ross, E. D. Identification of Low-Complexity Domains by Compositional Signatures Reveals Class-Specific Frequencies and Functions Across Reference Proteomes. Preprint at https://doi.org/10.1101/2023.07.24.550260 (2023).

23. Bevilacqua, P. C., Williams, A. M., Chou, H.-L. & Assmann, S. M. RNA multimerization as an organizing force for liquid–liquid phase separation. *RNA* **28**, 16–26 (2022).

24. Sharif, H. *et al*. Structural analysis of the yeast Dhh1–Pat1 complex reveals how Dhh1 engages Pat1, Edc3 and RNA in mutually exclusive interactions. *Nucleic Acids Res.* (2013) doi:10.1093/nar/gkt600.

25. Sachdev, R. *et al*. Pat1 promotes processing body assembly by enhancing the phase separation of the DEAD-box ATPase Dhh1 and RNA. *eLife* **8**, e41415 (2019).

26. Terry, S. C., Jerman, J. H. & Angell, J. B. A gas chromatographic air analyzer fabricated on a silicon wafer. *IEEE Trans. Electron Devices* **26**, 1880–1886 (1979).

27. Harrison, D. J. *et al*. Micromachining a Miniaturized Capillary Electrophoresis-Based Chemical Analysis System on a Chip. *Science* **261**, 895–897 (1993).

28. Duffy, D. C., McDonald, J. C., Schueller, O. J. A. & Whitesides, G. M. Rapid Prototyping of Microfluidic Systems in Poly(dimethylsiloxane). *Anal. Chem.* **70**, 4974–4984 (1998).

29. Battat, S., Weitz, D. A. & Whitesides, G. M. An outlook on microfluidics: the promise and the challenge. *Lab. Chip* **22**, 530–536 (2022).

Bibliography

30.   Teh, S.-Y., Lin, R., Hung, L.-H. & Lee, A. P. Droplet microfluidics. *Lab. Chip* **8,** 198 (2008).

31.   Li Jeon, N. *et al*. Neutrophil chemotaxis in linear and complex gradients of interleukin-8 formed in a microfabricated device. *Nat. Biotechnol*. **20**, 826–830 (2002).

32.   Sackmann, E. K., Fulton, A. L. & Beebe, D. J. The present and future role of microfluidics in biomedical research. *Nature* **507**, 181–189 (2014).

33.   Schindelin, J. *et al*. Fiji: an open-source platform for biological-image analysis. *Nat. Methods* **9**, 676–682 (2012).

34.   Stirling, D. R. *et al*. CellProfiler 4: improvements in speed, utility and usability. *BMC Bioinformatics* **22**, 433 (2021).

35.   Design of Experiments - File Exchange - OriginLab. https://www.originlab.com/fileExchange/details.aspx?fid=462.

36.   Linsenmeier, M. *et al*. Dynamics of Synthetic Membraneless Organelles in Microfluidic Droplets. *Angew. Chem. Int. Ed*. **58**, 14489–14494 (2019).

37.   Frenz, L., Blank, K., Brouzes, E. & Griffiths, A. D. Reliable microfluidic on-chip incubation of droplets in delay-lines. *Lab Chip* **9**, 1344–1348 (2009).

38.   Belousov, K. I. *et al*. An asymmetric flow-focusing droplet generator promotes rapid mixing of reagents. *Sci. Rep*. **11**, 8797 (2021).

39.   McIntyre, D., Lashkaripour, A., Arguijo, D., Fordyce, P. & Densmore, D. Versatility and stability optimization of flow-focusing droplet generators *via* quality metric-driven design automation. *Lab. Chip* **23**, 4997–5008 (2023).

Appendix

Droplet Generation and LLPS

µl	Compound
100	LSB_MS_00
20	BSA 10 mg/mL
40	ATP pH 6.4
20	PolyU
80	MilieQ
100	Phosphate Buffer 10 mM pH 6.4
360	

Appendix Table 1: Master mix used for the LLPS assay with pMH1674, pMH1930 and pMH1931.

Buffer Recipes

NaCl conc [M]	MgCl conc. [M]	LSB_MS_00	LSB_MS_50	LSB_MS_100	BSA 10mg/ml	ATP 10mM	polyA	polyU	EA-Buffer	Milli Q	100 mM Phosphate pH=6.4
0.15	0.002	0	20	0	4	8	0	2	2	16	0
0.1	0.002	20	0	0	4	16	0	4	0	8	0
0.1	0.002	20	0	0	4	16	0	0	4	8	20
0.2	0.002	0	0	20	4	0	0	0	4	24	0
0.2	0.002	0	0	20	4	0	0	4	0	24	20
0.15	0.002	20	0	0	4	0	0	0	4	24	20
0.1	0.002	20	0	0	4	0	0	0	4	24	0
0.1	0.002	20	0	0	4	16	0	4	0	8	20
0.2	0.002	0	0	20	4	16	0	0	4	8	20
0.2	0.002	0	20	0	4	8	0	2	2	16	0
0.15	0.002	0	0	20	4	0	0	0	4	24	20
0.15	0.002	0	0	20	4	0	0	4	0	24	0
0.1	0.002	0	0	20	4	16	0	0	4	8	0
0.1	0.002	20	0	0	4	0	0	4	0	24	20
0.2	0.002	20	0	0	4	0	0	4	0	24	0
0.2	0.002	0	0	20	4	16	0	4	0	8	20
0.15	0.002	20	0	0	4	16	0	0	4	8	0
0.1	0.002	0	0	20	4	16	0	4	0	8	0
0.2	0.002	0	20	0	4	8	0	2	2	16	0

Appendix Table 2: An overview of the DoE done for the LLPS assay, including concentrations of all Master mix combinations.

1 L MH1000G Tris pH = 8.0 Buffer (Binding Buffer)

1. 58.44 g / 200 mL NaCl 5 M Stock solution
2. 50 mL Tris pH = 8.0 (1 M)
3. 126 g / 100 mL Glycerol
4. 25 mM Imidazole
5. Filled up to 1 L with Milli-Q water
6. Adjust pH if needed

Appendix

7. Filter and Degas

1 L MH1000G Tris pH = 7.5 Buffer (Dialysis Buffer)

1. 58.44 g / 200 mL NaCl 5 m Stock solution
2. 50 mL Tris pH = 7.5 (1 M)
3. 126 g / 100 mL Glycerol
4. 25 mM Imidazole
5. Filled up to 1 L with Milli-Q water
6. 206 µl of 2-Mercaptoethanol (14.5 M)
7. 2 mM $MgCl_2$

1 L MH1000G Phosphate pH = 7.5 (Size Exclusion Buffer)

1. 58.44 g / 200 mL NaCl 5 m Stock solution
2. 50 mL Phosphate pH = 7.5 (1 M)
3. 126 g / 100 mL Glycerol
4. Filled up to 1 L with Milli-Q water
5. 206 µl of 2-Mercaptoethanol (14.5 M)
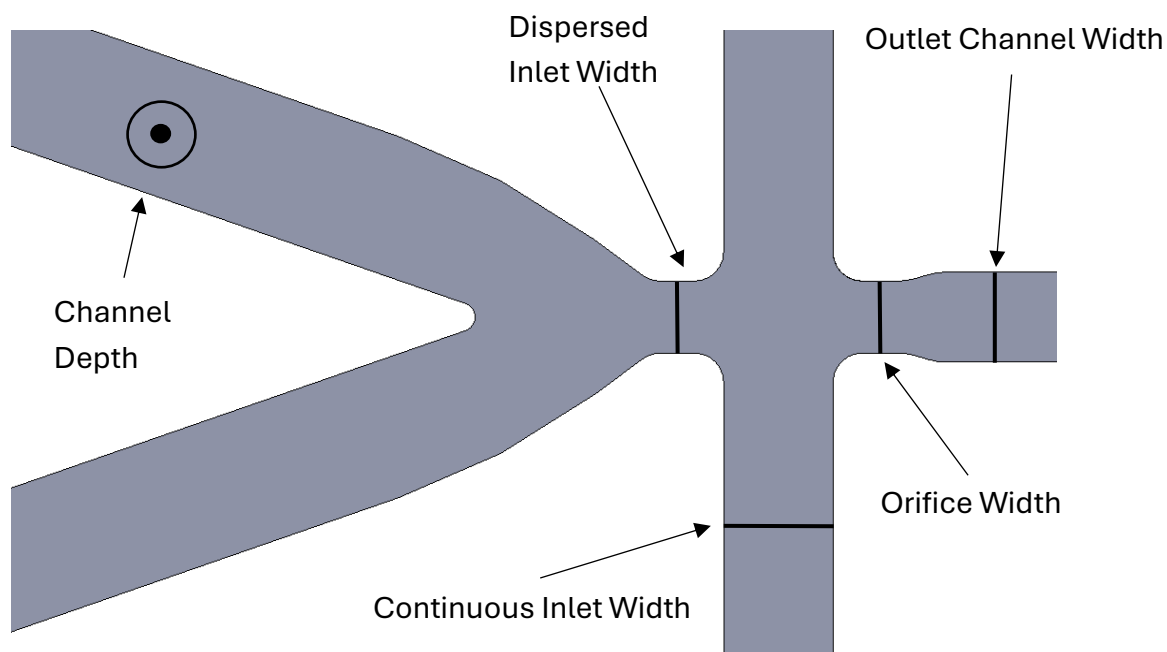6. 2 mM $MgCl_2$

900 mL Terrific Broth

1. 12 g Tryptone
2. 24 g yeast extract
3. 880 mL MiliQ water
4. 20 mL Glycerole (25% v/v)

1 L Lysogeny Broth

1. 10 g Tryptone
2. 5 g yeast extract
3. 10 g Sodium Chloride
4. 1000 mL MiliQ water

Appendix

Chip Measurements

Appendix Figure 1: A schematic representation of the droplet generator used in the redesigned chip design.

	Orifice Width (µm)	Channel Depth (µm)	Outlet Channel Width (µm)	Dispersed Inlet Width (µm)	Continuous Inlet Width (µm)	Droplet Diameter (µm)	Oil Flow (µl/h)	Trigger & Protein Flow (µl/h)
135 Hz Chip	25	43.75	31.25	25	37.5	30	151	6.9
235 Hz Chip	25	43.75	31.25	25	31.25	30	227	12
500 Hz Chip	25	43.75	25	25	25	30	492	26

Appendix

1000 Hz Chip	25	43.75	31.25	31.25	25	30	758	50.8

Appendix Table 3: The exact measurements of the different chips and their predicted flow and droplet generation attributes.

Appendix
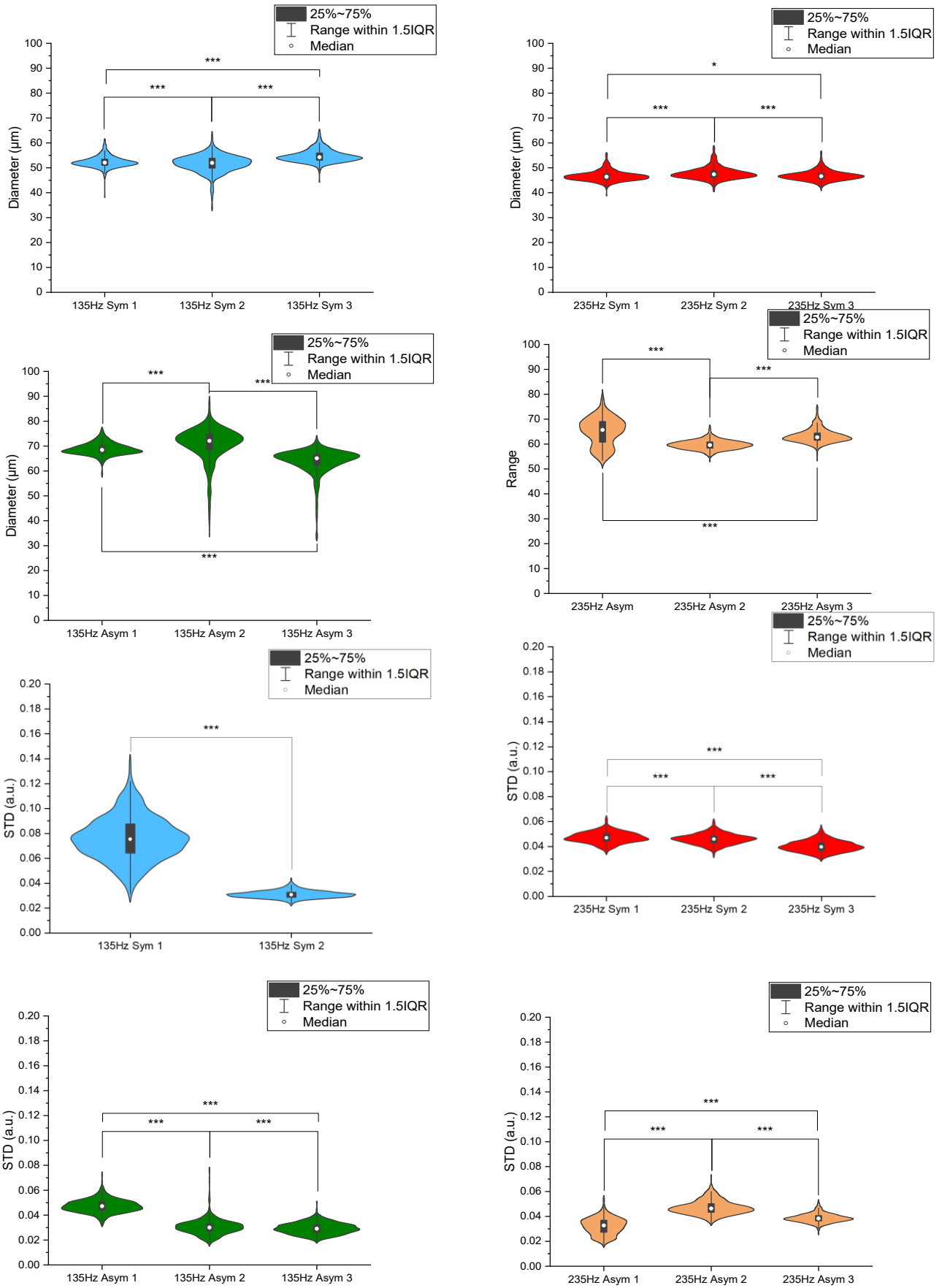
Appendix Figure 2: Violin plots showing all triplicate measurements in both diameter and homogeneity (Standard deviation of droplets). *** indicates a p-value of p<0.001. * indicates a p-value of p<0.05.

Appendix

CellProfiler Settings: Diameter, intensity

a

Select the input image GFP ⌄ (from NamesAndTypes)

Name the output image RescaleIntensityGFP

Rescaling method Stretch each image to use the full intensity range ⌄

Use advanced settings?	● Yes ○ No
Select the input image	RescaleIntensityGFP ⌄ (from RescaleIntensity #05)
Name the primary objects to be identified	Droplets
Typical diameter of objects, in pixel units (Min,Max)	40 300
Discard objects outside the diameter range?	● Yes ○ No
Discard objects touching the border of the image?	● Yes ○ No
Threshold strategy	Adaptive ⌄
Thresholding method	Otsu ⌄
Two-class or three-class thresholding?	Three classes ⌄
...ssign pixels in the middle intensity class to the foreground or the background?	Background ⌄
Threshold smoothing scale	10
Threshold correction factor	0.75
Lower and upper bounds on threshold	0 1
Size of adaptive window	250
Log transform before thresholding?	○ Yes ● No
Method to distinguish clumped objects	Shape ⌄
Method to draw dividing lines between clumped objects	Shape ⌄
Automatically calculate size of smoothing filter for declumping?	○ Yes ● No
Size of smoothing filter	25
Automatically calculate minimum allowed distance between local maxima?	○ Yes ● No
Suppress local maxima that are closer than this minimum allowed distance	50
Speed up by using lower-resolution image to find local maxima?	● Yes ○ No
Display accepted local maxima?	○ Yes ● No
Fill holes in identified objects?	After declumping only ⌄
Handling of objects if excessive number of objects identified	Continue ⌄

Select the objects to filter Droplets ⌄ (from IdentifyPrimaryObjects #06)

Name the output objects FilterDroplets

Select the filtering mode Measurements ⌄

Select the filtering method Limits ⌄

Category: AreaShape ⌄

Select the measurement to filter by Measurement: FormFactor ⌄

Filter using a minimum measurement value? ● Yes ○ No

Minimum value 0.8

Filter using a maximum measurement value? ○ Yes ● No

Add another measurement

Keep removed objects as a separate set? ○ Yes ● No

Relabel additional objects to match the filtered object? Add an additional object

☑ Droplets   (from IdentifyPrimaryObjects #06)

Select object sets to measure

Calculate the Zernike features? ● Yes ○ No

alculate the advanced features? ○ Yes ● No

Select images to measure

☐ GFP   (from NamesAndTypes)
☑ RescaleIntensityGFP   (from RescaleIntensity #05)

Select objects to measure

☐ Droplets   (from IdentifyPrimaryObjects #06)
☑ FilterDroplets   (from FilterObjects #10)

Calculate intensity Zernikes? None ⌄

Select images to measure

☐ GFP   (from NamesAndTypes)
☑ RescaleIntensityGFP   (from RescaleIntensity #05)

Select objects to measure FilterDroplets ⌄ (from FilterObjects #10)

Object to use as center? These objects ⌄

Add another object

Scale the bins? ● Yes ○ No

Number of bins 4

Add another set of bins

Add another heatmap display

Appendix

b

Choose a tracking method Distance

Select the objects to track FilterObjects (from FilterObjects #08)

Maximum pixel distance to consider matches 20

Filter objects by lifetime? ● Yes ○ No

Filter using a minimum lifetime? ● Yes ○ No

Minimum lifetime 10

Filter using a maximum lifetime? ○ Yes ● No

Select display option Color and Number

Save color-coded image? ● Yes ○ No

Name the output image TrackedDroplets

Select the input image GFP (from NamesAndTypes)

Name the output image RescaleIntensityGFP

Rescaling method Stretch each image to use the full intensity range

Appendix

Use advanced settings?	● Yes ○ No
Select the input image	RescaleIntensityGFP ▾ (from RescaleIntensity #05)
Name the primary objects to be identified	Droplets
Typical diameter of objects, in pixel units (Min,Max)	150 500
Discard objects outside the diameter range?	● Yes ○ No
Discard objects touching the border of the image?	● Yes ○ No
Threshold strategy	Adaptive ▾
Thresholding method	Otsu ▾
Two-class or three-class thresholding?	Three classes ▾
ssign pixels in the middle intensity class to the foreground or the background?	Background ▾
Threshold smoothing scale	10
Threshold correction factor	0.75
Lower and upper bounds on threshold	0 1
Size of adaptive window	250
Log transform before thresholding?	○ Yes ● No
Method to distinguish clumped objects	Shape ▾
Method to draw dividing lines between clumped objects	Shape ▾
Automatically calculate size of smoothing filter for declumping?	○ Yes ● No
Size of smoothing filter	25
Automatically calculate minimum allowed distance between local maxima?	○ Yes ● No
Suppress local maxima that are closer than this minimum allowed distance	50
Speed up by using lower-resolution image to find local maxima?	● Yes ○ No
Display accepted local maxima?	○ Yes ● No
Fill holes in identified objects?	After declumping only ▾
Handling of objects if excessive number of objects identified	Continue ▾

Appendix

Select the input objects Droplets ∨ (from IdentifyPrimaryObjects #06)

Name the output objects bigger

Select the operation Expand objects by a specified number of pixels ∨

Number of pixels by which to expand or shrink 20

☐ Droplets   (from IdentifyPrimaryObjects #06)
☑ bigger   (from ExpandOrShrinkObjects #07)

Select object sets to measure

Calculate the Zernike features? ⦿ Yes ○ No

Calculate the advanced features? ○ Yes ⦿ No

Select the objects to filter | bigger ∨ | (from ExpandOrShrinkObjects #07)

Name the output objects | FilterDroplets

Select the filtering mode | Measurements ∨

Select the filtering method | Limits ∨

Select the measurement to filter by

Category: | AreaShape ∨

Measurement: | FormFactor ∨

Filter using a minimum measurement value? | ● Yes ○ No

Minimum value | 0.75

Filter using a maximum measurement value? | ○ Yes ● No

Add another measurement

Keep removed objects as a separate set? | ○ Yes ● No

Relabel additional objects to match the filtered object? | Add an additional object

Select object sets to measure

☐ Droplets | (from IdentifyPrimaryObjects #06)
☑ FilterDroplets | (from FilterObjects #10)
☐ bigger | (from ExpandOrShrinkObjects #07)

Calculate the Zernike features? | ● Yes ○ No

Calculate the advanced features? | ○ Yes ● No

Select the input image Protein ∨ (from NamesAndTypes)

Name the output image RescaleIntensityProtein

Rescaling method Stretch each image to use the full intensity range ∨

Select images to measure
- ☐ GFP (from NamesAndTypes)
- ☑ Protein (from NamesAndTypes)
- ☐ RescaleIntensityGFP (from RescaleIntensity #05)
- ☐ RescaleIntensityProtein (from RescaleIntensity #12)

Select objects to measure
- ☐ Droplets (from IdentifyPrimaryObjects #06)
- ☑ FilterDroplets (from FilterObjects #10)
- ☐ bigger (from ExpandOrShrinkObjects #07)

*Appendix Figure 3: The relevant exact settings of the CellProfiler pipeline for measurements of **a**. droplet diameter, intensity, **b**. velocity (Only the track objects module is shown, all other settings are identical to **a**.) and the pipeline for **c**. LLPS in capillaries.*

Appendix

University of Basel
Faculty of Science

Declaration on Scientific Integrity
(including a Declaration on Plagiarism and Fraud)
Translation from German original

Title of Thesis: The influence of RNA-RNA Interaction on the Formation
Kinetics of Biomolecular Condensates ⊞

Name Assessor: Prof. Maria Hondele

Name Student: Jonas Keller

Matriculation No.: 17-056-730

I attest with my signature that I have written this work independently and without outside help. I also attest that the information concerning the sources used in this work is true and complete in every respect. All sources that have been quoted or paraphrased have been marked accordingly.

Additionally, I affirm that any text passages written with the help of AI-supported technology are marked as such, including a reference to the AI-supported program used. This paper may be checked for plagiarism and use of AI-supported technology using the appropriate software. I understand that unethical conduct may lead to a grade of 1 or "fail" or expulsion from the study program.

Place, Date: 21.10.2024   Student: _Z. Keller_

Will this work, or parts of it, be published?

☐ No

☑ Yes. With my signature I confirm that I agree to a publication of the work (print/digital) in the library, on the research database of the University of Basel and/or on the document server of the department. Likewise, I agree to the bibliographic reference in the catalog SLSP (Swiss Library Service Platform). (cross out as applicable)

Publication as of: 31.10.2024

Place, Date: 21.10.2024   Student: _Z. Keller_

Place, Date: _____   Assessor: _M. Hondele_

Please enclose a completed and signed copy of this declaration in your Bachelor's or Master's thesis.

September 2023